Liu Qiao (Orcid ID: 0000-0002-9039-9160)

Impacts of Multi-timescale Circulations on Meridional Heat Transport

Qiao LIU[1, 2], Tim LI[3, 1*], and Weican ZHOU[1, 4]

1 Collaborative Innovation Center on Forecast and Evaluation of Meteorological Disasters (CIC-FEMD) / Key Laboratory of Meteorological Disaster, Ministry of Education (KLME) / Joint International Research Laboratory of Climate and Environmental Change (ILCEC), Nanjing University of Information Science and Technology, Nanjing 210044, China

2 Anhui Meteorological Observatory, Hefei 230031, China

3 International Pacific Research Center and Department of Atmospheric Sciences, School of Ocean and Earth Science and Technology, University of Hawaii at Manoa, Honolulu, HI 96822, USA

4 Suqian Zeda Vocational and Technical College, Suqian 223808, China

Corresponding author: Tim Li, Department of Atmospheric Sciences, School of Ocean and Earth Science and Technology, University of Hawaii at Manoa, Honolulu, Hawaii 96822. Email: timli@hawaii.edu

This is the author manuscript accepted for publication and has undergone full peer review but has not been through the copyediting, typesetting, pagination and proofreading process, which may lead to differences between this version and the Version of Record. Please cite this article as doi: 10.1002/joc.7357

ABSTRACT

Relative contributions to the zonal mean meridional heat transport by the climatological annual mean, climatological annual variation, synoptic, intra-seasonal, and lower-frequency motions were examined based on the ERA-Interim reanalysis data for the period of 1981-2015. The meridional heat transport analyzed in this study only includes the component related to meridional wind and temperature. In the tropics, the climatological annual mean circulations dominate the long-term mean meridional heat transport, while the interaction between the climatological annual mean temperature and the seasonal anomalous flow largely contributes to the seasonal variation of the meridional heat transport. In the middle latitudes, the climatological annual mean circulations and transient eddies (mostly synoptic and intra-seasonal eddies) are of roughly equal importance in the poleward heat transport, leading to the maximum poleward heat transport around 50°N/S. The upper- and lower-tropospheric heat transports by the climatological annual mean circulations appear opposite, with the magnitude of the lower-tropospheric transport being greater. The preferred maximum zonal mean heat transport at 50°N by the climatological mean flow is attributed to the maximum zonal mean low-level southerly in situ. The preferred peak latitude of the mid-latitude poleward heat transport by synoptic eddies near 50°N arises from the combined effect of the strong synoptic-scale meridional wind and temperature variabilities in situ and their in-phase relationship. The heat transport by tropical cyclones (TCs) was estimated by applying a statistical relationship between TC intensity and the vertically integrated temperature averaged over the TC core region derived from high-resolution Weather Research and Forecasting (WRF) model simulations. For northern hemisphere summer, TCs contribute about 35% of the total heat transport in the active TC regions, suggesting that TCs play a critical role in the regional meridional heat transport.

Key words: meridional heat transport by multi-timescale motions, TC-induced heat transport

1. Introduction

The primary driver of the global climate system is solar radiation. Due to the differences between the absorbed sunlight and the heat radiated into space, there is a net energy surplus in the tropics and a net energy deficit in the polar regions. To balance the heat surplus and deficit and maintain a quasi-steady climate state, meridional heat transport by the atmosphere and oceans must occur. Many previous studies have estimated the zonal mean meridional atmosphere and ocean heat transports (e.g., Houghton 1954; Vonder Haar and Oort 1973; Oort and Haar Vonder 1976; Hsiung 1985; Masuda 1988; Hsiung et al. 1989; Messori and Czaja 2013; Armour et al. 2019). It was shown that the atmosphere is the major poleward heat transport agent poleward of 30° (Czaja and Marshall 2006), while the meridional ocean heat transport is comparable to the transport in the atmosphere between 10°S and 10°N (Trenberth et al. 2019). The meridional heat transport by atmospheric circulations plays a key role in reaching the equilibrium state of the Earth climate.

Previous studies mostly decomposed the heat transport into the contribution by the time and zonal mean circulations, stationary eddies, and transient eddies (e.g., Peixoto and Oort 1992; Zhu and Newell 1998). It was noted that the atmospheric heat transport in the tropics is primarily controlled by the mean meridional circulations (i.e., the Hadley Cells; Hadley 1735), while the poleward heat transport by transient eddies is stronger in the mid and high latitudes (Peixoto and Oort 1992; Oort and Peixoto 1983; Barry et al. 2002; Yang et al. 2015). The largest contribution from transient eddies to the atmospheric heat transport arises from the lower troposphere (say, at 850 hPa) (Lau 1978; Peixoto and Oort 1992). However, relative contributions from the synoptic, intra-seasonal and lower-frequency motions to the poleward heat transport in the mid and high latitudes remain unclear.

The atmospheric heat transport in climate models was examined in various previous studies (e.g., Donohoe and Battisti 2012; Donohoe et al. 2013; Yang et al. 2015; Feldl and Bordoni 2016). Donohoe et al. (2013) suggested that the seasonal cycle of the location of the Intertropical Convergence Zone was highly anti-correlated with the atmospheric heat transport at the equator in both observations and 16 models in the Coupled Model Intercomparison Project phase 3 (CMIP3) multi-model database. Yang et al. (2015)

separated the atmospheric heat transport into a mean component and an eddy component using the Community Earth System Model (version 1.0) and found that the dry static energy transport by eddy activities accounted for more than 50% of the total transport in the middle latitudes. Moreover, some attention was paid to the changes of atmospheric heat transport in the warmer climate (Held and Soden 2006; Langen and Alexeev 2007; Graversen et al. 2011; Zelinka and Hartmann 2012). Zelinka and Hartmann (2012) revealed that greater poleward energy transport is required on a warming planet in a suite of global climate models from CMIP3. To understand climate change more clearly, a detailed understanding of the atmospheric heat transport by different timescale motions is needed.

As intensive weather systems, tropical cyclones (TCs) may exert a significant impact on the Earth's climate (Emanuel 2001, 2005; Kossin et al. 2007). In a parallel study, we examined the TC-induced poleward moisture transport (Liu et al. 2021) and found that TCs might contribute about 28% of the total moisture transport over the western North Pacific (WNP). The role of Atlantic hurricanes in meridional heat transport was examined by Hu and Meehl (2009). They found that strong hurricane winds could strengthen the Atlantic meridional overturning circulation, leading to increased northward heat transport in a state-of-the-art global coupled climate model (CCSM3). As TCs transport heat poleward during the poleward movement, it is critical to understand the role of TCs in the global and regional meridional heat transport.

The total atmospheric energy is defined as the sum of four major components: internal energy, latent heat, geopotential energy and kinetic energy (e.g., Mayer and Haimberger 2012; Liu et al. 2020). In this study, we only focus on the atmospheric heat transport associated with temperature and intend to investigate the relative importance of different timescale motions contributing to the zonal mean meridional heat transport. The meridional heat transport by TCs will also be examined. As the temperature in the TC warm core region is often underestimated in the coarse-resolution reanalysis data (Zick and Matyas 2015), we intend to estimate the TC-induced heat transport by using a more realistic temperature profile in the TC core region derived from a large number of high-resolution Weather Research and Forecasting (WRF) model simulations. The data and methods used in this study are described in Section 2. Relative contributions by the climatological annual

mean, climatological annual variation, synoptic, intra-seasonal, and lower-frequency motions to the zonal mean meridional heat transport are assessed in Section 3. The causes of the maximum zonal mean heat transport by synoptic eddies are discussed in Section 4. The seasonal variation of the meridional heat transport is examined in Section 5. In Section 6, the poleward heat transport by TCs is analyzed. Finally, Section 7 summarizes the key findings.

2. Data and methodology

a. Data

The meridional heat transport is computed by using the daily wind and temperature fields from the European Centre for Medium-Range Weather Forecasts (ECMWF) Interim reanalysis (ERA-Interim; Dee et al. 2011) at 19 isobaric levels from 1000 to 100 hPa at a 50-hPa interval. The horizontal resolution of the dataset is 1.5°×1.5°. The analysis in this study covers a period from 1981 to 2015. TC information comes from the International Best Track Archive for Climate Stewardship (IBTrACS; Knapp et al. 2010).

b. Decomposition of the meridional heat flux into different timescales

The vertically integrated atmospheric meridional heat flux, denoted by HF, is expressed as:

$$\overline{HF} = \overline{\frac{1}{g}\int_{P_{top}}^{P_{bot}} vT\,dp}\ , (1)$$

where v denotes the meridional wind, T denotes the temperature, $g = 9.8\ m\ s^{-2}$ is the gravitational acceleration, P_{bot} represents the closest pressure level to the surface, and $P_{top} = 100\ hPa$ denotes the top of the troposphere. HF is computed by using the meridional wind and temperature fields in the reanalysis data and the unit of HF is K kg m^{-1} s^{-1}. The overbar denotes the time average. To account for the changes of mass due to the curvature of the earth, the vertically integrated heat flux is weighted by latitudes (multiply by $cos(\varphi)$). φ denotes the latitude.

We use the Fourier analysis technique (Saltsman 1957) and the Lanczos filter (Duchon 1979) to separate the original meridional wind and temperature fields into different

timescale components. The Fourier analysis technique is applied to the 35-year averaged daily data (with 365 days) to obtain the climatological annual mean component (0 harmonic) and the climatological annual variation component (1-4 harmonics), respectively. Then, we use the Lanczos filter to separate the anomalous field which has been derived by removing the climatological annual mean and annual variation components from the 35-year reanalysis data into a 10-day high-pass filtered field representing the synoptic-scale component, a 10–90-day band-pass filtered field representing the intra-seasonal component, and a lower-frequency (inter-annual or longer timescale) component. Thus, the temperature and meridional wind fields are separated into five portions in the frequency domain which can be written as $T = T_M + T_A + T_S + T_I + T_L$, (2) and $v = v_M + v_A + v_S + v_I + v_L$, (3). Subscripts represent the climatological annual mean (M), climatological annual variation (A), synoptic scale (S), intra-seasonal scale (I), and lower-frequency scale (L). Applying these definitions to calculating the meridional heat flux by different timescale motions, we obtain the following:

$$\overline{HF} = \overline{\frac{1}{g}\int_{P_{top}}^{P_{bot}}(v_M T_M + v_A T_A + v_S T_S + v_I T_I + v_L T_L)\, dp} + \overline{HF_R}, \quad (4)$$

where $v_M T_M$ represents the meridional heat flux contributed by the climatological annual mean circulations. $v_A T_A$, $v_S T_S$, $v_I T_I$, and $v_L T_L$ denote the contribution from the climatological annual variation, the synoptic-scale anomalies, the intra-seasonal anomalies, and the lower-frequency anomalies, respectively. HF_R represents the residual term, including the cross-timescale terms. HF_R is expected to be zero after taking the full-time mean (denoted by the overline) because of the orthogonal timescale decomposition methods.

c. Description of the WRF model

The WRF (Skamarock et al. 2008) model is used for TC numerical simulations. Three nested domains with the innermost domain moving with the storm are constructed and horizontal resolutions are 16 km, 8km and 2 km, respectively. The outermost domain covers a region within (100°E-180°E and 10°S-50°N). The Kain-Fritch convective scheme is applied to the outermost mesh. Other model physics include the Dudhia shortwave

radiation parameterization, the WRF-single moment 6-class (WSM6) microphysics scheme and the Rapid Radiative Transfer Model (RRTM) longwave radiation parameterization. National Centers for Environmental Prediction (NCEP) Final (FNL) Operational Global Analysis (available online at https://rda.ucar.edu/datasets/ds083.2/) data, with 1°×1° resolution, are used as the initial and boundary conditions in the numerical simulations.

3. Meridional heat transport by different timescale motions

The zonal mean meridional heat transport by different timescale motions is shown in Figure 1. The sum of the zonal mean meridional heat transport associated with the synoptic, intra-seasonal, lower-frequency, climatological annual variation and climatological annual mean components is in good agreement with the total heat transport. A small difference between the total heat flux and the sum of the five terms above is likely a numerical error due to the temporal filtering. The result implies that the contribution from the residual term ($\overline{HF_R}$) in Equation (4) is small and negligible. The dominant role of the climatological annual mean circulations in driving the zonal mean meridional heat transport in the tropics is evident in Figure 1a. It has been well documented that much of the heat transport is accomplished by the Hadley cells within the tropical latitudes (Peixoto and Oort 1992). To examine the contribution by the mean meridional circulations, we calculate the associated heat flux using the following formula:

$$\overline{HF_{MMC}} = \overline{\frac{1}{g}\int_{P_{top}}^{P_{bot}} \left(\left[\overline{V_M}\right]\left[\overline{T_M}\right]\right) dp}, \quad (5)$$

where HF_{MMC} represents the vertically integrated meridional heat flux contributed by the mean meridional circulations and the square bracket denotes the zonal mean. The mean meridional circulations largely contribute to the climatological annual mean component, illustrating the dominant role of the Hadley cells in the tropical zonal mean meridional heat transport. The meridional heat transport by the climatological annual mean circulations also plays the most important role in the mid-latitude poleward heat transport, followed by the contributions from the synoptic and intra-seasonal motions. The zonal mean heat flux associated with the climatological annual variation and lower-frequency components is near zero. A recent study (Liu et al. 2021) has shown that the synoptic and intra-seasonal

motions contribute to 80% of the maximum poleward moisture transport at 40°N/S. However, the zonal-mean poleward heat transport peaks occur at around 50°N/S, and the transient eddy (including the synoptic and intra-seasonal anomalies) and the annual cycle (including the climatological annual mean and annual variation) components are equally important to the poleward heat transport in the middle latitudes. The transient eddy and the annual cycle components account for 52% and 48% of the total meridional heat transport at 50°, respectively (Fig. 1b).

The horizontal patterns of the meridional heat transport by different timescale motions are shown in Figure 2. Two southwest-northeast oriented northward heat transport branches occur in the North Pacific and Atlantic (Fig. 2a). Strong southward heat transport centers are located in East Asia and North America. The heat flux in East Asia, the North Pacific, North America, and the North Atlantic (NA) shows a wave train pattern. Strong northward heat transport centers in the southern hemisphere (SH) occur in the mid-latitude South Atlantic basin and South Indian Ocean (SIO), and east of Australia, while the southward transport center is located to the south of Australia. The total meridional heat transport (Fig. 2a) is largely contributed by the climatological annual mean component (Fig. 2b). The magnitudes of the heat flux associated with other timescale motions (Figs. 2c-f) are much smaller than that of the climatological annual mean component due to the smaller magnitudes of different timescale temperature anomalies. The meridional heat transport associated with the climatological annual variation (Fig. 2c) is stronger in the northern hemisphere (NH) with strong northward transport over East Asia. Poleward heat transport by the synoptic (Fig. 2d) and intra-seasonal (Fig. 2e) motions occur in the middle latitudes of both hemispheres, with enhanced transport over storm tracks. Though the local heat flux associated with the climatological annual mean state is much greater than that by synoptic and intra-seasonal motions in the middle latitudes, transient eddies are as important as the climatological annual mean circulations in the mid-latitude zonal mean heat transport (Fig. 1). This is attributed to the cancellation of northward and southward transports by the mean flows across the latitude bands. The poleward lower-frequency heat transport (Fig. 2f) is relatively weak based on 35-year data, resulting in a quite small contribution to the zonal-mean meridional heat transport.

It is worth mentioning that there are a few caveats and biases that have been reported about the ERA-Interim data (e.g., Dee et al. 2011; Hersbach et al. 2020). Compared to the ERA-Interim, the ERA5 has an enhanced horizontal resolution of 31 km with the use of more observations such as hyperspectral data and ground-based radar data (Hersbach et al. 2019). The ERA5 also rectifies a problem with the earlier 1D+4D-Var assimilation of rain-affected radiances that led to anomalous precipitation in the ERA-Interim over the oceans in the 1990s (Dee et al. 2011; Hersbach et al. 2020). As a result, the ERA5 features a much-improved troposphere, and more consistent sea surface temperature and sea ice concentration (Hersbach and Dee 2016; Wang et al. 2019). To reveal how the current analysis result is sensitive to different reanalysis products, we conduct a parallel calculation of the meridional heat transport by different timescale motions with the higher-resolution (0.25°×0.25°) ERA5 reanalysis product (Fig. S1). The result is quite similar to Fig. 2 except that the magnitudes of the intra-seasonal and lower-frequency heat transport (Figs. S1d, f) are a little larger.

To examine the vertical distribution of the meridional heat transport in the middle latitudes, we plot the vertical profiles of the zonal mean meridional heat flux by different timescale motions at 50°N (Fig. 3a). The northward total heat transport decreases with height in the lower troposphere (P_{bot}-650 hPa), and southward total heat transport occurs in the upper troposphere (650-100 hPa) with the maximum transport at 200 hPa. The meridional heat transport by the climatological annual mean circulations has similar vertical distribution to the total transport. The mean meridional circulations are the largest contributor to the meridional heat transport associated with the climatological annual mean state (Fig. 1a). To examine the effect of the mean meridional circulations on the vertical distribution of the heat transport at 50°N, we plot the vertical profile of the zonal and annual mean meridional wind (Fig. 3b). The mean southerly in the lower layer and the mean northerly in the upper layer are consistent with the opposite meridional heat transport in the Ferrel Cell. We also compare the annual and zonal mean meridional wind and temperature fields at 850 hPa with that at 200 hPa in the NH (Fig. 3c). The zonal mean temperature at 200hPa and 850 hPa is greater than 220 K with a negative meridional temperature gradient at 850 hPa in the middle latitudes and a negligibly weak gradient at

200 hPa. Zonal mean northerlies occur in the equator and middle latitudes, while southerlies occur in the low latitudes at 850 hPa. The direction of the meridional wind at 200 hPa is opposite to that at 850 hPa, which is attributed to the three-cell meridional circulations known as the Hadley Cell, Ferrel Cell, and Polar Cell. Additionally, the maximum northerly occurs at around 15°N and the maximum southerly occurs at around 50°N at 850 hPa, which is consistent with the latitudinal locations of the maximum zonal-mean equatorward and poleward heat transports by the annual mean circulations (Fig. 1a). The vertically integrated heat flux associated with the annual mean circulations in the lower and upper troposphere is shown in Figure 3d. The heat transport by the annual mean circulations in the upper layer is opposite to that in the lower layer. As the climatological annual mean temperature decreases with height, the heat transport in the upper layer is offset by that in the lower layer and the vertically integrated heat flux is largely contributed by the lower troposphere. Different from the vertical distribution of the meridional heat transport by the climatological annual mean circulations, poleward heat transport by synoptic eddies occurs in both the upper and lower troposphere with the maximum transport in the lower troposphere (Fig. S2).

4. Causes of the maximum heat transport by synoptic eddies at 50°N or S

An interesting question is why the maximum zonal mean heat transport by synoptic eddies occurs near 50°N/S. As the synoptic-scale heat transport is greater in the lower troposphere (Fig. S2), we plot the horizontal maps of standard deviations of the 850-hPa synoptic-scale meridional wind [$\sigma(v_s)$] and temperature [$\sigma(T_s)$] fields and their correlation (Figs. 4a-c) to examine the relative roles of meridional wind and temperature anomalies in the mid-latitude poleward heat transport. It is note that the correlation coefficients between the synoptic meridional wind and temperature anomalies (Fig. 4c) are generally positive (negative) in the NH (SH). The in-phase relationship between the temperature anomalies and the poleward wind anomalies leads to the poleward heat transport at the synoptic scale. The variabilities of the synoptic-scale meridional wind and temperature are large in the middle latitudes with enhanced synoptic-scale activities over the storm track regions (Fig. 4a). The synoptic-scale temperature variabilities are also strong in East Asia and North

America (Fig. 4b).

In addition, to reveal the mechanism behind the synoptic poleward heat transport peak at around 50°N/S, the meridional profiles of the zonal mean standard deviations of the synoptic-scale meridional wind and temperature and their correlation in the NH are shown in Figures 4d-f. The maximum variabilities of the zonal-mean synoptic meridional wind and temperature occur at around 50°N, resulting in a maximum of their product at around 50°N. The correlation between the synoptic-scale meridional wind and temperature reaches a peak at 40°N and the positive correlation coefficient is large at 50°N. These lead to the peak latitude of the northward heat transport by the synoptic motion at around 50°N. The maximum variability of the synoptic meridional wind anomalies is primarily attributed to the mid-latitude atmospheric baroclinic instability, which is determined by either the vertical wind shear or meridional temperature gradient. From a potential vorticity (PV) point of view, the instability may also depend on atmospheric static stability (Grotjahn 2003; Robinson 2010). An Eady Growth Rate index was introduced to measure the strength of atmospheric baroclinic instability (Lindzen and Farrell 1980; Chu et al. 2020). It is given by:

$$I_B = 0.31f\frac{\left|\frac{\partial \overrightarrow{V_h}}{\partial z}\right|}{N}, \quad (6)$$

where f is the Coriolis parameter, $\overrightarrow{V_h}$ is the horizontal wind field, and N is the Brunt–Väisälä frequency. The zonal mean Eady Growth Rate index (red dashed curve in Fig. 4d) is found to peak south of the maximum variability of the 850-hPa synoptic-scale meridional wind (red solid curve in Fig. 4d). Atmospheric synoptic-scale perturbations are often enhanced to the northeast of the mid-latitude westerly jet in the jet exit region (Holton 2004; Diao et al. 2018), due to the geostrophic velocity and so induced vertical motion. As a result, the maximum synoptic-scale activity occurs to the north of the 200-hPa jet (blue curve in Fig. 4d). The latitudinal location of the maximum synoptic-scale temperature variability is consistent with the latitudinal location of the maximum product of the mean temperature gradient and the standard deviation of the synoptic meridional wind (Fig. 4e). Thus, the preferred latitudinal location of the maximum zonal mean meridional heat

transport by the synoptic-scale motion is largely attributed to the latitudinal locations of the maximum variability of the synoptic meridional wind associated with the mid-latitude baroclinic instability and the maximum variability of the synoptic temperature anomalies associated with the anomalous advection of the mean temperature.

An empirical orthogonal function (EOF) analysis is conducted to show the dominant modes of the 850-hPa synoptic-scale wind and temperature fields in the middle latitudes. The first leading EOF mode is shown in Figure 5. Mid-latitude synoptic-scale waves are evident over the North Pacific, North America, the Atlantic, the SIO, and the western South Pacific. The second mode has a similar wave like pattern to the first mode but with a 90-degree phase difference (figure not shown). The two leading modes capture about 12% of the total variance. The positive temperature anomalies are located at the east (west) of a synoptic-scale cyclonic (anti-cyclonic) circulation, while negative temperature anomalies are located at the west (east) of the cyclonic (anti-cyclonic) circulation. As the anomalous poleward flow transports warm air poleward, the temperature anomalies are in phase with the poleward wind anomalies. The anomalous advection of the mean temperature results in the poleward synoptic-scale heat transport in the middle latitudes.

Figure 6 shows the standard deviations of the meridional wind and temperature anomalies and their correlations associated with the intra-seasonal and lower-frequency timescales at 850 hPa. The in-phase relationship between the temperature anomalies and the anomalous poleward wind on the intra-seasonal/lower-frequency timescale is similar to the synoptic-scale counterpart and the correlation is as strong. The weaker intra-seasonal heat transport is due to the weaker variabilities of the meridional wind anomalies. Moreover, variabilities of both the lower-frequency meridional wind and temperature anomalies are extremely weak, leading to the negligible lower-frequency heat transport (Fig. 2f).

5. Seasonal variation of the meridional heat transport

Figure 7 shows the zonal mean meridional heat transport by various timescale components in northern winter (December–February, DJF) and summer (June-August, JJA), respectively. Similar to the seasonal mean moisture transport examined in Liu et al.

(2021), the contribution from the interactions between the climatological annual mean and the climatological annual variation to the seasonal mean heat transport is not negligible. Note that the seasonal reverse heat transport in the tropics (Figs. 7a, b) is largely contributed by the interaction between the mean temperature and the seasonal anomalous meridional wind which is related to the seasonal variation of the Hadley cells. The poleward heat transport in the mid-latitude NH in DJF is greater than that in JJA, which is attributed to the seasonal reverse heat transport by the interactions between the climatological annual mean and annual variation components. The relative contributions from different timescale components averaged at 50°N and 50°S are shown in Figures 7c-d. The annual cycle and transient eddy components play equally important roles in the mid-latitude seasonal mean heat transport. In DJF, the interactions between the climatological annual mean and annual variation components drive about 15% of the poleward heat transport, while equatorward transport due to the two interaction components occurs in JJA. This leads to the weaker poleward heat transport in JJA at 50°.

The horizontal patterns of the total meridional heat flux and the meridional heat flux due to the interaction between the mean temperature and the seasonal anomalous wind in boreal winter are shown in Figure 8. The horizontal pattern of the total heat transport in DJF (Fig. 8a) is similar to that of the long-term mean transport (Fig. 2a). The magnitude of the transport in DJF in the NH is stronger than the long-term mean transport, especially in East Asia, North America, the North Pacific, and the NA, resulting in a more obvious wave train pattern of the heat transport in the middle latitudes. The magnitude of the meridional heat transport of the mean temperature by the seasonal anomalous flow (Fig. 8b) is comparable to that by the mean flow (Fig. 2b). In addition, the horizontal pattern of the transport of the mean temperature by the seasonal anomalous wind in DJF in the NH is similar to that by the mean flow, resulting in the enhanced heat transport in DJF in the NH (Fig. 8a).

The climatological annual mean and annual variation components of the 850-hPa temperature and wind fields in DJF are plotted in Figs. 8c-d to understand the seasonal variation of the meridional heat transport. The maximum seasonal anomalous meridional wind at the equator (Fig. 8c) is related to Somali low-level jet. The mean northerlies in East

Asia and North America and the mean southerlies in the North Pacific and Atlantic associated with the mid-latitude cyclonic circulations (Fig. 8d) contribute to the wave train pattern of the heat transport in the mid-latitude NH (Fig. 2b). The anomalous cyclonic circulations in the North Pacific and Atlantic in DJF (Fig. 8c), which are caused by the land-ocean thermal contrast, enhance the wave train pattern.

The relative contributions of the climatological annual mean component and the interaction between the seasonal anomalous meridional wind and mean temperature to the wave train pattern of the total heat transport in DJF are shown in Figure 9. They appear roughly equally important. The averaged meridional heat flux in the key regions (black boxes in Fig. 8) is calculated by subtracting the negative box-averaged heat flux in the North Pacific and Atlantic from the positive box-averaged heat flux in North America and East Asia. The transport of the mean temperature by the seasonal anomalous wind is as important as the transport by the climatological annual mean wind. The transport of the seasonal anomalous temperature by the annual mean wind, on the other hand, is negligibly small in contributing to the wave train pattern.

6. Meridional heat transport by TCs

TCs are unique weather systems with positive-only temperature distribution and poleward movement, which differs considerably from the synoptic-scale eddies that have both positive and negative meridional wind and temperature components. As such, the zonal average of the synoptic-scale meridional wind or temperature is zero across a latitudinal band. Therefore, the heat transport by TCs deserves a specific section to discuss, and it cannot be simply regarded as a part of the synoptic-scale contribution.

As TCs transport heat poleward during their poleward movement, the total meridional heat transport by TCs is defined as:

$$\overline{HF_{TC}} = \overline{\frac{1}{g}\int_{P_{top}}^{P_{bot}} C_T T_T \, dp} \, , (7)$$

where C_T is the meridional moving speed of a TC calculated by using the TC best track data from the IBTrACS and T_T is the total temperature averaged within a 500-km radius from the TC center. The TC-induced heat transport is calculated based on TC moving speed

and temperature averaged within the TC core region. TCs with the tropical depression category or above (i.e., maximum wind greater than 21 knots) are considered in this study.

Given the unique poleward heat transport feature of TCs, a part of TC meridional heat transport may be included in the annual mean component. As reanalysis products always underestimate TC warm core intensity, we develop an approach to construct a statistical relationship between the vertically integrated temperature in the TC inner core region and TC intensity by using outputs from the WRF model. 100 TC cases in the WNP during JASO for the period of 2000-2008 are simulated. The positive relationship between the TC warm core strength and the TC minimum sea level pressure is shown in Figure 10. The linear regression equation is represented by:

$$\langle T_T \rangle = -0.0046 p_{min} + 249.6, \quad (8)$$

where $\langle T_T \rangle$ is the vertically integrated temperature of a TC averaged within a 500-km radius from the TC center and p_{min} is the minimum sea level pressure of the TC. The unit of $\langle T_T \rangle$ is 10^4 K kg m^{-2} and the unit of p_{min} is hPa. Then we apply this linear relationship to Equation (7) and obtain the heat transport by TCs as following:

$$\overline{HF_{TC}} = \overline{\frac{1}{g} C_T \langle T_T \rangle} = \overline{\frac{1}{g} C_T (-0.0046 p_{min} + 249.6)}, \quad (9)$$

As most of TCs form in July to October (JASO) in the NH and in January to April (JFMA) in the SH, we only focus on the heat transport by TCs during active TC seasons. Horizontal patterns of the TC meridional heat transport during JASO and JFMA 1981-2015 are shown in Figure 11. The poleward heat transport by TCs in the NH is consistent with the poleward TC tracks, with maximum centers in the WNP, eastern North Pacific (ENP), NA, SIO, Australia, and South Pacific (SP) basins. The zonal mean heat transport by TCs is shown in Figure 11c, which displays that the TC northward (southward) heat transport peaks at around 20°N (20°S) in JASO (JFMA). The magnitude of the poleward TC heat transport is larger in JASO than in JFMA. Area-averaged meridional heat flux by TCs and the total meridional heat flux in active TC regions (black boxes in Figs. 11a, b) during JASO and JFMA are listed in Table 1. The TC-induced heat flux and the total heat flux in the TC active regions in the NH in JFMA are positive and TC contributes about 35% of the total heat transport, indicating the important role of TCs in the regional heat transport.

However, positive and negative total heat flux cancel each other in the active TC regions in the SH, resulting in the relatively weak area-averaged heat transport.

7. Conclusion

Although the zonal mean heat transport by the mean flow and eddies was investigated previously, the relative contributions to the transport by different timescale motions such as synoptic, intra-seasonal and lower-frequency motions are not clear. By separating the wind and temperature fields into the climatological annual mean, annual variation, synoptic, intra-seasonal and lower-frequency components, relative contributions from different timescale motions to the zonal mean meridional heat transport are evaluated based on the 35-year ERA-Interim reanalysis data. In the tropics, the annual mean circulations dominate the long-term mean meridional heat transport. In the middle latitudes, the mean circulations and the synoptic and intra-seasonal eddies are equally important to the poleward heat transport. Compared to the moisture transport that peaks at 40°N/S (Liu et al. 2021), the maximum heat transport occurs at around 50°N/S. While the synoptic and intra-seasonal motions contribute most of the moisture transport in mid-latitudes (Liu et al. 2021), they only contribute about a half of the total heat transport at 50°N/S.

Different from the zonal mean moisture transport that is confined in the low level, the zonal mean heat transport in the lower troposphere has an opposite sign to the upper troposphere and the magnitude of the transport in the lower troposphere is greater. As a result, part of the lower-tropospheric heat transport offsets the upper-tropospheric counterpart. The zonal mean meridional heat transport by the climatological annual mean circulations has a peak at 50°N, being consistent with the maximum zonal and annual mean poleward wind at 850 hPa. The poleward heat transport by synoptic-scale motions also has a peak slightly south of 50°N. It is partially attributed to the in-phase relationship between the synoptic-scale temperature and poleward wind anomalies. Besides, the maximum variability of the synoptic-scale meridional wind in the NH occurs at around 50°N, due to the mid-latitude baroclinic instability. Meanwhile, the combined effect of the strong synoptic meridional wind variability and the strong meridional gradient of the mean temperature leads to the maximum synoptic temperature variability slightly south of 50°N.

Both the maximum temperature and meridional wind variabilities and their in-phase relationship lead to the peak synoptic-scale heat transport at around 50°N. It is worth mentioning that the dominant mode of the 850-hPa synoptic-scale wind field in the middle latitudes has a typical zonal wavelength of 1000-6000 km. This implies that spatial scales are somewhat linked to temporal scales, and a realistic zonal wavelength can be achieved with the current synoptic-scale temporal filtering. Although the temperature anomalies are also in phase with the poleward wind anomalies at the intra-seasonal timescale, the magnitude of the intra-seasonal meridional wind variabilities is smaller compared to the synoptic-scale counterpart. This leads to a weaker intra-seasonal heat transport. Moreover, the lower-frequency meridional wind and temperature variabilities are much weaker compared to the synoptic and intra-seasonal counterparts. As a result, the lower-frequency motion has a negligible contribution to the zonal mean meridional heat transport. There is limitation in the current examination of the lower-frequency heat transport by using 35-year reanalysis data.

The interaction between the climatological annual mean temperature and the seasonal anomalous flow leads to the seasonal reverse of the zonal mean heat transport in the tropics, with southward (northward) heat transport in DJF (JJA). This is largely attributed to the seasonal change of the Hadley cells. The poleward heat transport by the interactions between the climatological annual mean and annual variation contributes about 15% of the total heat transport averaged at 50° in DJF, while the equatorward heat transport by the two interaction components is offset by the transient eddy and the annual cycle components in JJA. As a result, the mid-latitude heat transport is stronger in DJF in the NH.

The ERA-Interim reanalysis still suffered from mass imbalance (Berrisford et al., 2011). In order to obtain reasonable and meaningful meridional heat transport from reanalysis and avoid spurious sinks and sources, it is essential to first identify mass residual and correct the mass budget (Trenberth 1991; Trenberth and Solomon 1994; Mayer et al. 2017; Liu et al. 2020). Trenberth (1991) developed a method to correct the mass budget by adjusting the barotropic wind and the method was improved in subsequent studies (Trenberth et al. 1995; Trenberth and Fasullo 2018). However, the mass residual issue is not considered in the current study. As we average the heat transport at different timescales

and latitudes, the imbalance becomes not so dominant and noticeable.

As important synoptic weather systems, TCs have a unique feature in comparison with the conventional synoptic eddies. TCs have positive-only poleward heat transport, whereas synoptic-scale waves can transport heat either poleward or equatorward. The synoptic heat transport does not consist of realistic TC contribution. Given the underestimated warm core of TCs in the reanalysis products, we estimate TC-induced heat transport based on high-resolution WRF model simulations of 100 TCs in the WNP during JASO 2000-2008. A statistical relationship between the TC intensity and the vertically integrated temperature averaged in the TC core region is derived. Thus, the meridional heat transport by TCs during active TC seasons is obtained by using the best track data from the IBTrACS. It is found that the maximum poleward heat transport by TCs occurs at around 20°N/S and the transport in the NH is greater than that in the SH. TCs contribute about 35% of the total meridional heat transport averaged over the active TC regions in the NH, indicating that TCs play an important role in the regional meridional heat transport. The limitation of the TC-induced heat transport is that axisymmetric horizontal distributions of TC wind and temperature fields are not considered and the statistical relationship between TC intensity and temperature is established only based on the WNP TC cases.

Acknowledgements. This work is jointly supported by NSFC Grant 42088101, NOAA NA18OAR4310298, NSF AGS-2006553. This is SOEST contribution number 12345, IPRC contribution number 1234, and ESMC number 123.

REFERENCES

Armour, K.C., Siler, N., Donohoe, A. and Roe, G.H. (2019) Meridional atmospheric heat transport constrained by energetics and mediated by large-scale diffusion. *J. Climate*, 32, 3655-3680. https://doi.org/10.1175/JCLI-D-18-0563.1.

Barry, L., Craig, G. and Thuburn, J. (2002) Poleward heat transport by the atmospheric heat engine. *Nature,* 415, 774-777. https://doi.org/10.1038/415774a.

Berrisford, P., Kållberg, P., Kobayashi, S., et al. (2011) Atmospheric conservation properties in ERA‐Interim. *Q. J. R. Meteorol. Soc.*, 137, 1381–1399. https://doi.org/10.1002/qj.864.

Chu, C., Hu, H., Yang, X. Q. and Yang, D.J. (2020) Midlatitude atmospheric transient eddy feedbacks influenced ENSO-associated wintertime Pacific teleconnection patterns in two PDO phases. *Climate Dyn.,* 54, 2577–2595. https://doi.org/10.1007/s00382-020-05134-4.

Czaja, A. and Marshall, J. (2006) Partitioning of poleward heat transport between the atmosphere and ocean. *J. Atmos. Sci.*, 63, 1498-1511. https://doi.org/10.1175/JAS3695.1.

Dee, D.P. and Coauthors (2011) The ERA-interim reanalysis: configuration and performance of the data assimilation system. *Quart. J. Roy. Meteor. Soc.*, 137, 553-597. https://doi.org/10.1002/qj.828.

Diao, Y.F., Li, T. and Hsu, P.C. (2018) Influence of the Boreal Summer Intraseasonal Oscillation on Extreme Temperature Events in the Northern Hemisphere. *J. Meteor. Res.*, 32, 534-547. https://doi.org/10.1007/s13351-018-8031-8.

Donohoe, A. and Battisti, D.S. (2012) What determines meridional heat transport in climate models? *J. Climate,* 25, 3832-3850. https://doi.org/10.1175/JCLI-D-11-00257.1.

Donohoe, A., Marshall, J.C., Ferreira, D. and Mcgee, D. (2013) The relationship between ITCZ location and cross-equatorial atmospheric heat transport: from the seasonal cycle to the last glacial maximum. *J. Climate*, 26, 3597-3618. https://doi.org/10.1175/JCLI-D-12-00467.1.

Duchon, C.E. (1979) Lanczos filtering in one and two dimensions. *J. Appl. Meteor.*, 18, 1016-1022. https://doi.org/10.1175/1520-0450(1979)018<1016:LFIOAT>2.0.CO;2.

Emanuel, K.A. (2001) Contribution of tropical cyclones to meridional heat transport by the oceans. *J. Geophys. Res.*, 106, 14,771-14,781. https://doi.org/10.1029/2000JD900641.

Emanuel, K.A. (2005) Increasing destructiveness of tropical cyclones over the past 30 years. *Nature*, 436, 686-688. https://doi.org/10.1038/nature03906.

Feldl, N. and Bordoni, S. (2016) Characterizing the Hadley circulation response through regional climate feedbacks. *J. Climate*, 29, 613-622. https://doi.org/10.1175/JCLI-D-15-0424.1.

Graversen, R.G., Mauritsen, T., Drijfhout, S., Tjernstrom, M. and Martensson, S. (2011) Warm winds from the Pacific caused extensive Arctic sea-ice melt in summer 2007. *Climate Dyn.,* 36, 2103-2112. https://doi.org/10.1007/s00382-010-0809-z.

Grotjahn, R. (2003) Baroclinic instability. *Encyclopedia of Atmospheric Sciences*., 179-188. https://doi.org/10.1016/B0-12-227090-8/00076-2.

Hadley, G. (1735) Concerning the cause of the general trade-winds. *Phil. Trans. R. Soc.*, 39, 58-62. https://doi.org/10.1098/rstl.1735.0014.

Held, I.M. and Soden, B.J. (2006) Robust responses of the hydrological cycle to global warming. *J. Climate*, 19, 5686-5699. https://doi.org/10.1175/JCLI3990.1.

Hersbach, H. and Dee, D. (2016) ERA5 reanalysis is in production, *ECMWF Newsletter*, 147. available at: https://www.ecmwf.int/en/newsletter/147/news/era5-reanalysis-production.

Hersbach, H., Bell, W., Berrisford, P., et al. (2019) Global reanalysis: goodbye ERA-Interim, hello ERA5. *ECMWF Newsletter*, 159, 17 – 24. https://doi.org/10.21957/vf291hehd7.

Hersbach, H., Bell, B., Berrisford, P., et al. (2020) The ERA5 global reanalysis. *Q. J. R. Meteorol. Soc.*, 146, 1999-2049. https://doi.org/10.1002/qj.3803.

Holton, J.R. (2004) *An Introduction to Dynamic Meteorology*. Academic Press, 535pp.

Houghton, H. (1954) On the annual heat balance of the northern hemisphere. *J. Meteorol.*, 11, 1-9. https://doi.org/10.1175/1520-0469(1954)011<0001:OTAHBO>2.0.CO;2.

Hsiung, J. (1985) Estimates of global oceanic meridional heat transport. *J. Phys. Oceanogr.*, 15, 1405–1413. https://doi.org/10.1175/1520-0485(1985)015<1405:EOGOMH>2.0.CO;2.

Hsiung, J., Newell, R.E. and Houghtby, T. (1989) The annual cycle of oceanic heat storage and oceanic meridional heat transport. *Quart. J. Roy. Meteor. Soc.*, 115, 1-28. https://doi.org/10.1002/qj.49711548502.

Hu, A. and Meehl, G.A. (2009) Effect of the Atlantic hurricanes on the oceanic meridional overturning circulation and heat transport. *Geophys. Res. Lett.*, 36, L03702. https://doi.org/10.1029/2008gl036680.

Knapp, K.R., Kruk, M.C., Levinson, D.H., Diamond, H.J. and Neumann, C.J. (2010) The international best track archive for climate stewardship (ibtracs). *Bull. Amer. Meteor. Soc.*, 91, 363-376. https://doi.org/10.1175/2009BAMS2755.1.

Kossin, J.P., Knapp, K.R., Vimont, D.J., Murnane, R.J. and Harper, B.A. (2007) A globally consistent reanalysis of hurricane variability and trends. *Geophys. Res. Lett.*, 34, L04815. https://doi.org/10.1029/2006GL028836.

Langen, P.L. and Alexeev, V.A. (2007) Polar amplification as a preferred response in an idealized aquaplanet GCM. *Climate Dyn.,* 29, 305-317. https://doi.org/10.1007/s00382-006-0221-x.

Lau, N.C. (1978) On the three-dimensional structure of the observed transient eddy statistics of the Northern Hemisphere wintertime circulation. *J. Atmos. Sci.*, 35, 1900-1923. https://doi.org/10.1175/1520-0469(1978)035<1900:OTTDSO>2.0.CO;2.

Lindzen, R.S., Farrell, B. (1980) A simple approximate result for the maximum growth rate of baroclinic instability. *J. Atmos. Sci*., 37, 1648–1654. https://doi.org/10.1175/1520-0469(1980)037<1648:ASARFT>2.0.CO;2.

Liu, Q., Li, T. and Zhou, W.C. (2021) Impacts of multi-timescale circulations on meridional moisture transport. In press.

Liu, Y., Attema, J., Moat, B. and Hazeleger, W. (2020) Synthesis and evaluation of historical meridional heat transport from midlatitudes towards the Arctic. *Earth System Dynamics Discussions*, 11, 77-96. https://doi.org/10.5194/esd-2019-17.

Masuda, K. (1988) Meridional heat transport by the atmosphere and the ocean: analysis of FGGE data. *Tellus*, 40A, 285-302. https://doi.org/10.1111/j.1600-0870.1988.tb00348.x.

Mayer, M., Haimberger, L., Edwards, J.M. and Hyder, P. (2017) Toward consistent diagnostics of the coupled atmosphere and ocean energy budgets. *J. Climate*, 30,

9225-9246. https://doi.org/10.1175/JCLI-D-17-0137.1.Messori, G. and Czaja, A. (2013) On the sporadic nature of meridional heat transport by transient eddies. *Quart. J. Roy. Meteor. Soc.*, 139, 999-1008. https://doi.org/10.1002/qj.2011.

Oort, A. and Vonder Haar, T.H. (1976) On the observed annual cycle in the ocean–atmosphere heat balance over the Northern Hemisphere. *J. Phys. Oceanogr.*, 6, 781–800. https://doi.org/10.1175/1520-0485(1976)006<0781:OTOACI>2.0.CO;2

Oort, A. and Peixoto, J. (1983) Global angular momentum and energy balance requirements from observations. *Adv. Geophys.*, 25, 355-490. https://doi.org/10.1016/S0065-2687(08)60177-6.

Peixoto, J. and Oort, A. (1992) *Physics of Climate*. American Institute of Physics Press, 520 pp.

Robinson, W.A. (2010) On the structure of potential vorticity in baroclinic instability. *Tellus Series A-dynamic Meteorology & Oceanography*, 41A(4). https://doi.org/275-284.10.1111/j.1600-0870.1989.tb00382.x.

Saltsman, B. (1957) Equations governing the energetics of the larger scales of atmospheric turbulence in the domain of wave number. *J. Atmos. Sci.*, 14, 513-523. https://doi.org/10.1175/1520-0469(1957)0142.0.CO;2.

Skamarock, W. C., and Coauthors, 2008: *A description of the Advanced Research WRF Version 3 (No. NCAR/TN-475+STR).* University Corporation for Atmospheric Research.113 pp, https://doi.org/10.5065/D68S4MVH.

Trenberth, K.E. (1991) Climate diagnostics from global analyses: Conservation of mass in ECMWF analyses. *J. Climate*, 4, 707–722. https://doi.org/10.1175/1520-0442(1991)004,0707: CDFGAC.2.0.CO;2.

Trenberth, K.E. and Solomon, A. (1994) The global heat balance: Heat transports in the atmosphere and ocean. *Climate Dyn.*, 10, 107–134. https://doi.org/10.1007/BF00210625.

Trenberth, K.E. and Fasullo, J.T. (2018) Applications of an updated atmospheric energetics formulation. *J. Climate*, 31, 6263-6279. https://doi.org/10.1175/JCLI-D-17-0838.1.

Trenberth, K.E., Hurrell, J.W. and Solomon, A. (1995) Conservation of mass in three dimensions in global analyses. *J. Climate*, 8, 692–708. https://doi.org/10.1175/1520-0442(1995)008,0692:COMITD.2.0.CO;2.

Trenberth, K.E., Zhang, Y., Fasullo, J. T. and Cheng, L. (2019) Observation-based estimates of global and basin ocean meridional heat transport time series. *J. Climate*, 32, 4567-4583. https://doi.org/10.1175/JCLI-D-18-0872.1.

Vonder Haar, T.H. and Oort, A.H. (1973) A new estimate of annual poleward energy transport by the oceans. *J. Phys. Oceanogr*., 3, 169–172. https://doi.org/10.1175/1520-0485(1973)003<0169:NEOAPE>2.0.CO;2.

Wang, C., Graham, R.M., Wang, K., et al. (2019) Comparison of ERA5 and ERA-Interim near surface air temperature and precipitation over Arctic sea ice: Effects on sea ice thermodynamics and evolution. *The Cryosphere*, 13, 1661 – 1679. https://doi.org/10.5194/tc-13-1661-2019.

Yang, H.J., Li, Q., Wang, K., Sun, Y. and Sun, D.X. (2015) Decomposing the meridional heat transport in the climate system. *Climate Dyn.*, 44, 2751-2768. https://doi.org/10.1007/s00382-014-2380-5.

Zelinka, M.D. and Hartmann, D. L. (2012) Climate feedbacks and their implications for poleward energy flux changes in a warming climate. *J. Climate*, 25, 608-624. https://doi.org/10.1175/JCLI-D-11-00096.1.

Zick, S.E. and Matyas, C.Z. (2015) Tropical cyclones in the North American Regional Reanalysis: An assessment of spatial biases in location, intensity, and structure. *J. Geophys. Res. Atmos.*, 120, 1651-1669. https://doi.org/10.1002/2014JD022417.

Zhu, Y. and Newell, R.E. (1998) A proposed algorithm for moisture fluxes from atmospheric rivers. *Mon. Wea. Rev.*, 126, 725-735. https://doi.org/10.1175/1520-0493(1998)1262.0.CO;2.

TABLE 1 Box-averaged total meridional heat flux (HF_{total}, unit: 10^4 K kg m^{-1} s^{-1}) and heat flux by TCs (HF_{TC}, unit: 10^4 K kg m^{-1} s^{-1}) in several TC active regions (black boxes in Fig. 11) in JASO and JFMA.

Season	region	Total heat flux HF_{total}	Heat flux by TCs HF_{TC}
JASO	WNP	147.8	42.8
	ENP	14.7	36.8
	NA	82.3	27.4
	WNP, ENP, and NA	100.9	35.2
JFMA	SIO	-0.2	-24.9
	SP	6.5	-18.5
	Australia	-10.8	-16.4
	SIO, Australia, and SP	1.0	-20.2

List of Figures

FIGURE 1 (a) Zonal mean meridional heat flux (unit: 10^4 K kg m^{-1} s^{-1}) associated with different timescale motions. The black solid curve denotes the total heat flux. The blue, red, brown, green, orange, purple curves denote the contribution by the climatological annual mean (M), annual variation (A), synoptic-scale (S), intraseasonal-scale (I), lower-frequency (L) motions, and the mean meridional circulations, respectively. The black dashed curve represents the sum of the five components (M, A, S, I, and L). (b) Meridional heat flux and relative percentage contributions by the annual cycle (climatological annual mean and annual variation, yellow) and the transient eddy (synoptic and intra-seasonal anomalies, gray) components at 50° (average at 50°N and 50°S). The black bar denotes the total heat flux.

FIGURE 2 (a) Vertically integrated annual mean meridional heat flux (unit: 10^4 K kg m^{-1} s^{-1}) during 1981-2015. (b)-(f) As in (a) except for the meridional heat flux by (b) the climatological annual mean, (c) annual variation, (d) synoptic, (e) intra-seasonal, and (f) lower-frequency motions.

FIGURE 3 Vertical profiles of (a) the zonal mean meridional heat flux (unit: 10^4 K kg m^{-1} s^{-1}) by different timescale modes and (b) the zonal and annual mean meridional wind (unit: m s^{-1}) at 50°N. Meridional profiles of (c) the climatological annual mean meridional wind (red, unit: m s^{-1}) and temperature (blue, unit: K) at 850 hPa (solid curve) and 200 hPa (dashed curve) in the NH and (d) the vertically integrated meridional heat flux (unit: 10^4 K kg m^{-1} s^{-1}) by the climatological annual mean circulations (black) and the vertically integrated heat flux in the upper troposphere (blue, 650-100 hPa) and the lower troposphere (red, P_{bot}-650 hPa) in the NH. The black curve in (a) denotes the total heat flux. The blue, red, brown, green, and orange curves in (a) denote the contribution by the climatological annual mean, annual variation, synoptic-scale, intra-seasonal, and lower-frequency motions, respectively.

FIGURE 4 Standard deviations of (a) the 850-hPa synoptic-scale meridional wind (unit: m s^{-1}) and (b) temperature (unit: K), and (c) correlation between the 850-hPa synoptic meridional wind and temperature anomalies. Meridional profiles of (d) the standard deviation of the 850-hPa synoptic-scale meridional wind (red solid curve), the

climatological annual-mean zonal wind at 200 hPa (blue curve), and the Eady Growth Rate index (red dashed curve, 10^{-6} s^{-1}), (e) standard deviation of the 850-hPa synoptic-scale temperature (red) and anomalous meridional advection of the mean temperature (blue, unit: 10^{-6} K s^{-1}), and (f) product (blue**,** unit: K m s^{-1}) of the standard deviations of the 850-hPa synoptic-scale meridional wind and temperature and correlation (red) between the 850-hPa synoptic meridional wind and synoptic temperature anomalies**.** Regions exceeding a 99% confidence level are shaded in (c).

FIGURE 5 Horizontal patterns of the 850-hPa wind (vector, unit: m s^{-1}) and temperature (shaded, unit: K) fields regressed onto the standardized time series of the leading EOF mode of the 850-hPa synoptic-scale meridional wind in the 30°-60° latitudinal band.

FIGURE 6 As in Figure 4 (a)-(c) except for (left) the intra-seasonal and (right) lower-frequency modes.

FIGURE 7 As in Figure 1 except for the vertically integrated seasonal mean meridional heat flux in (a, c) DJF and (b, d) JJA. The purple curve and bar denote the heat flux associated with the interaction between the seasonal anomalous meridional wind and the climatological annual mean temperature ($v_A T_M$), the pink curve and bar denote the heat flux associated with the interaction between the climatological annual mean meridional wind and the seasonal anomalous temperature ($v_M T_A$), and the black dashed curve represents the sum of the seven components (M, A, S, I, L, $v_A T_M$, and $v_M T_A$)**.**

FIGURE 8 (a) Vertically integrated seasonal mean meridional heat flux (unit: 10^4 K kg m^{-1} s^{-1}) in DJF during 1981-2015. (b) As in (a) except for the heat flux due to the interaction between the seasonal anomalous meridional wind and the climatological annual mean temperature. Horizontal patterns of the 850-hPa (c) seasonal anomalous wind (vector, unit: m s^{-1}) in DJF and the climatological annual mean temperature (shaded, unit: K) and (d) climatological annual mean wind (vector, unit: m s^{-1}) and the seasonal anomalous temperature (shaded, unit: K) in DJF. The black boxes in (a, b) represent the key regions for the wave train pattern of the meridional heat transport in the mid-latitude NH.

FIGURE 9 Averaged meridional heat flux (unit: 10^4 K kg m^{-1} s^{-1}) and relative percentage contributions by the climatological annual mean circulations (blue), the interaction between the climatological annual mean meridional wind and the seasonal anomalous temperature

(pink), and the interaction between the climatological annual mean temperature and the seasonal anomalous meridional wind (purple) in the four key regions (black boxes in Figure 8) for the wave train pattern of the meridional heat transport in the NH in DJF. The black bar denotes the averaged total heat flux.

FIGURE 10 Scatter diagrams between the vertically integrated temperature (unit: 10^4 K kg m^{-2}; red dots) averaged within a 500-km radius from the TC center and the TC minimum sea level pressure (unit: hPa). The slope of the linear regression line (black line) exceeds a 99% confidence level based on Student's t-test.

FIGURE 11 Horizontal patterns of the vertically integrated TC-induced heat flux (unit: 10^4 K kg m^{-1} s^{-1}) in (a) JASO and (b) JFMA 1981-2015. (c) Zonal mean meridional heat flux by TCs in JASO (red) and JFMA (blue). The black boxes in (a, b) represent the major regions for TC heat transport in the WNP (10ºN-40ºN, 115ºE-165ºE), ENP (10ºN-25ºN, 135ºW-100ºW), NA (10ºN-45ºN, 85ºW-40ºW), SIO (10ºS-40ºS, 40ºE-75ºE), Australia (10ºS-30ºS, 95ºE-125ºE), and SP (10ºS-40ºS, 155ºE-155ºW).

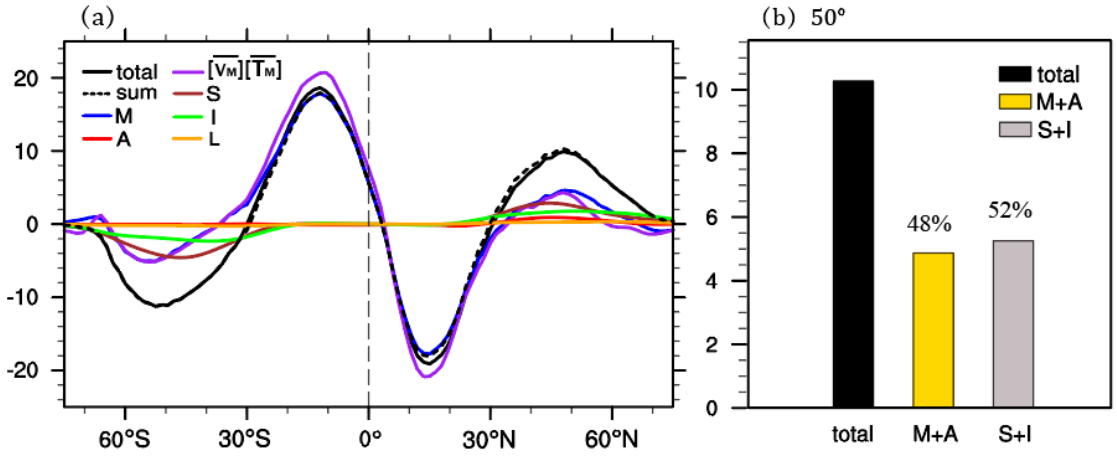

FIGURE 1 (a) Zonal mean meridional heat flux (unit: 10^4 K kg m^{-1} s^{-1}) associated with different timescale motions. The black solid curve denotes the total heat flux. The blue, red, brown, green, orange, purple curves denote the contribution by the climatological annual mean (M), annual variation (A), synoptic-scale (S), intraseasonal-scale (I), lower-frequency (L) motions, and the mean meridional circulations, respectively. The black dashed curve represents the sum of the five components (M, A, S, I, and L). (b) Meridional heat flux and relative percentage contributions by the annual cycle (climatological annual mean and annual variation, yellow) and the transient eddy (synoptic and intra-seasonal anomalies, gray) components at 50° (average at 50°N and 50°S). The black bar denotes the total heat flux.

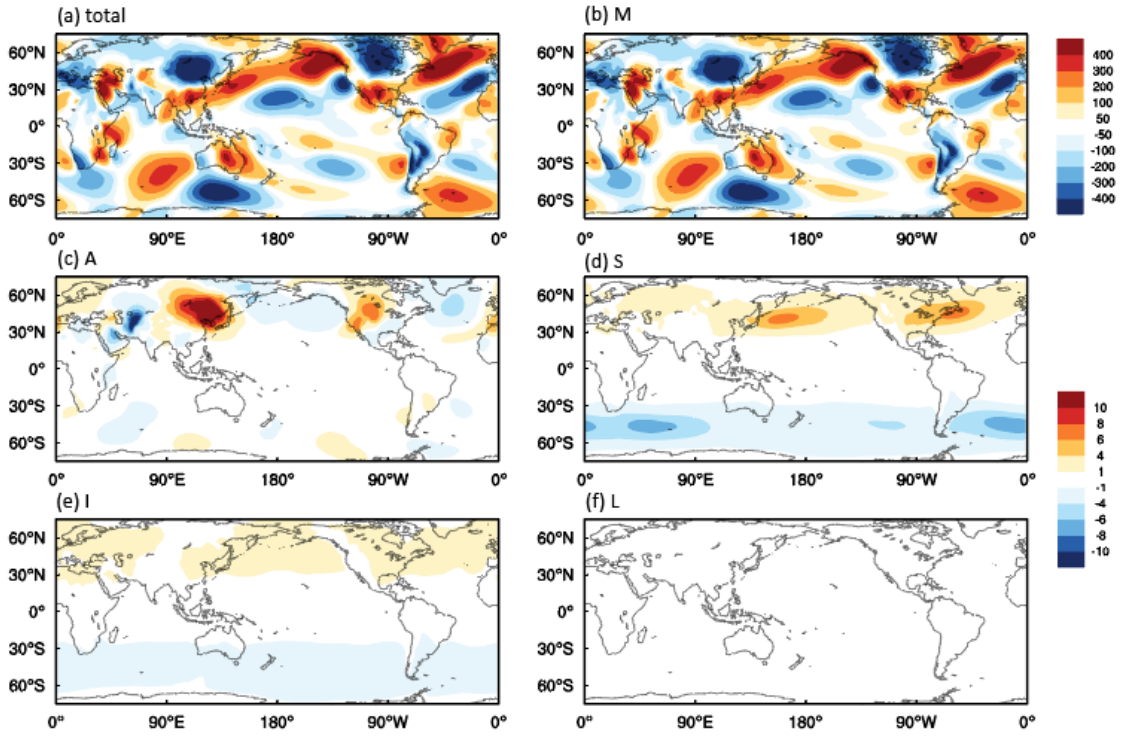

FIGURE 2 (a) Vertically integrated annual mean meridional heat flux (unit: 10^4 K kg m^{-1} s^{-1}) during 1981-2015. (b)-(f) As in (a) except for the meridional heat flux by (b) the climatological annual mean, (c) annual variation, (d) synoptic, (e) intra-seasonal, and (f) lower-frequency motions.

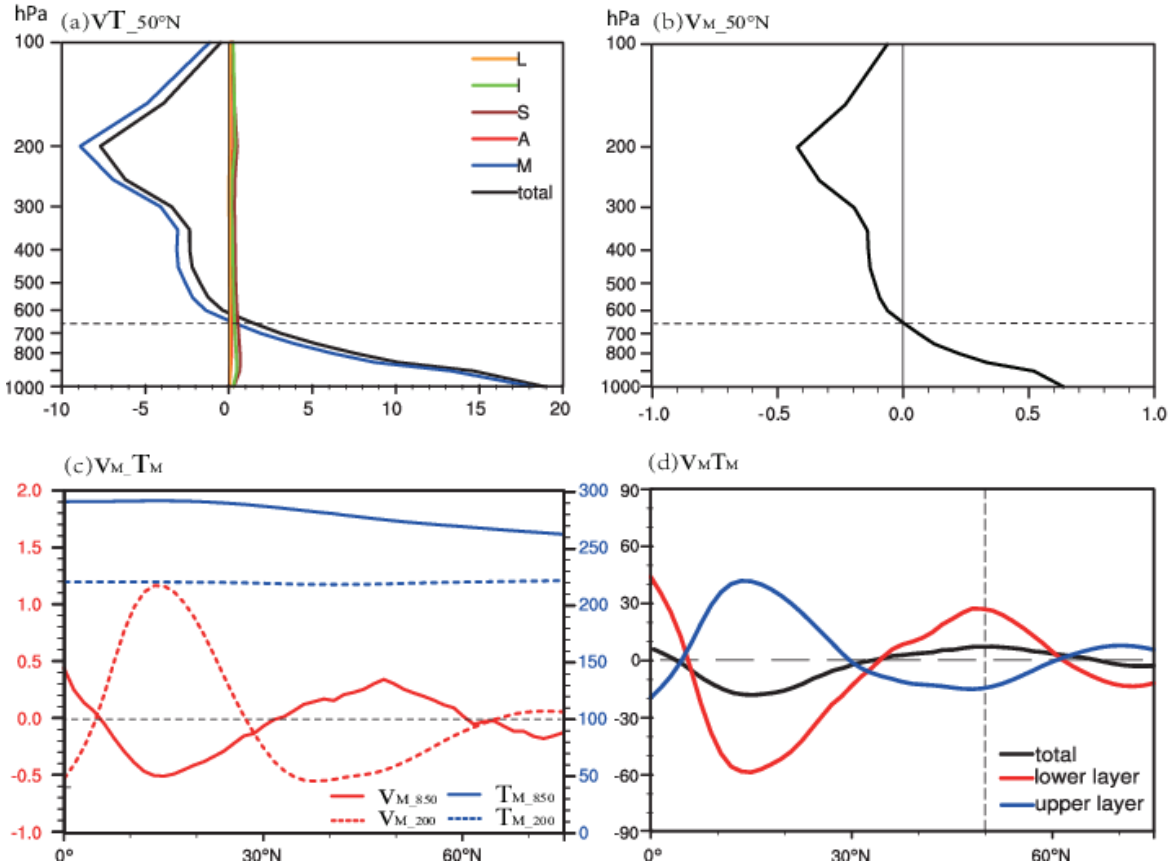

FIGURE 3 Vertical profiles of (a) the zonal mean meridional heat flux (unit: 10^4 K kg m^{-1} s^{-1}) by different timescale modes and (b) the zonal and annual mean meridional wind (unit: m s^{-1}) at 50°N. Meridional profiles of (c) the climatological annual mean meridional wind (red, unit: m s^{-1}) and temperature (blue, unit: K) at 850 hPa (solid curve) and 200 hPa (dashed curve) in the NH and (d) the vertically integrated meridional heat flux (unit: 10^4 K kg m^{-1} s^{-1}) by the climatological annual mean circulations (black) and the vertically integrated heat flux in the upper troposphere (blue, 650-100 hPa) and the lower troposphere (red, P_{bot}-650 hPa) in the NH. The black curve in (a) denotes the total heat flux. The blue, red, brown, green, and orange curves in (a) denote the contribution by the climatological annual mean, annual variation, synoptic-scale, intra-seasonal, and lower-frequency motions, respectively.

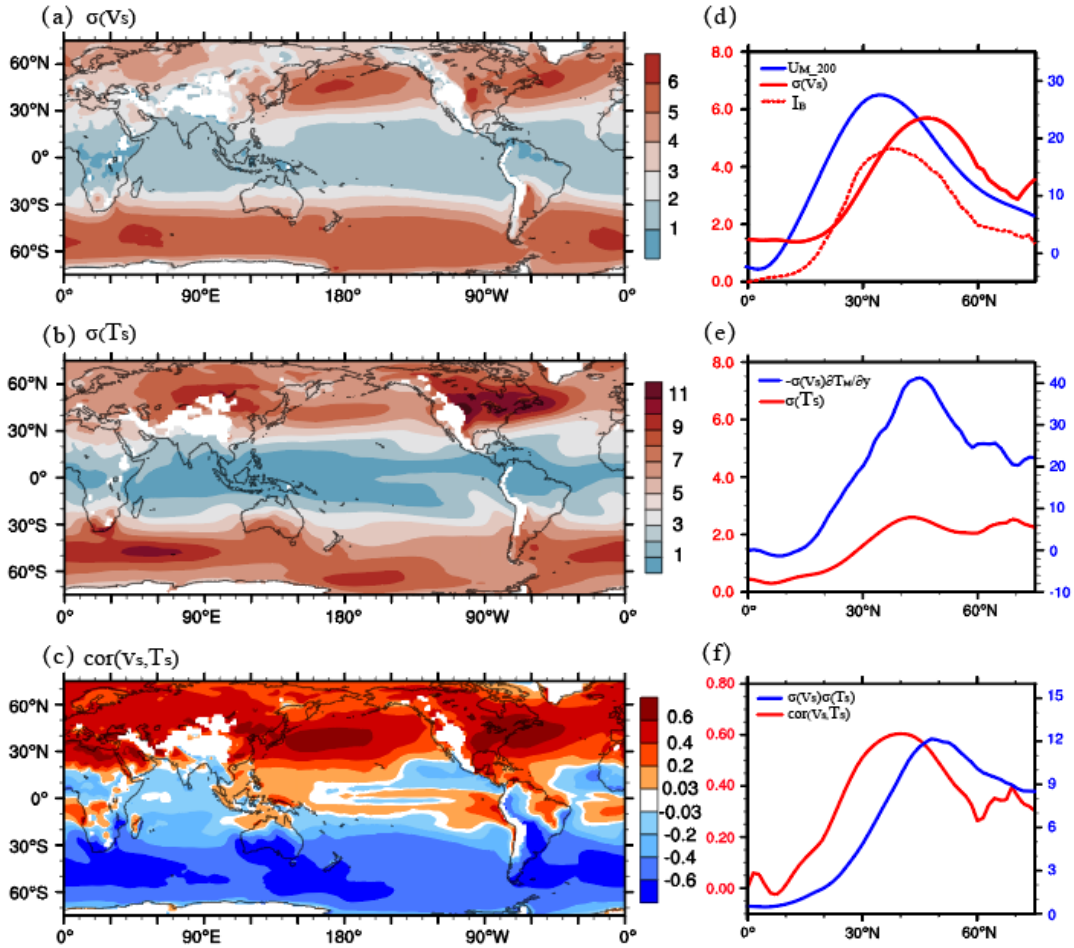

FIGURE 4 Standard deviations of (a) the 850-hPa synoptic-scale meridional wind (unit: m s^{-1}) and (b) temperature (unit: K), and (c) correlation between the 850-hPa synoptic meridional wind and temperature anomalies. Meridional profiles of (d) the standard deviation of the 850-hPa synoptic-scale meridional wind (red solid curve), the climatological annual-mean zonal wind at 200 hPa (blue curve), and the Eady Growth Rate index (red dashed curve, 10^{-6} s^{-1}), (e) standard deviation of the 850-hPa synoptic-scale temperature (red) and anomalous meridional advection of the mean temperature (blue, unit: 10^{-6} K s^{-1}), and (f) product (blue**,** unit: K m s^{-1}) of the standard deviations of the 850-hPa synoptic-scale meridional wind and temperature and correlation (red) between the 850-hPa synoptic meridional wind and synoptic temperature anomalies**.** Regions exceeding a 99% confidence level are shaded in (c).

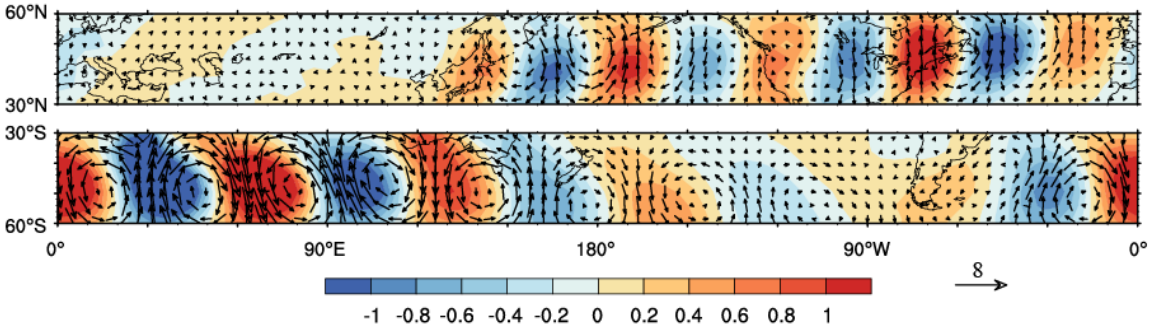

FIGURE 5 Horizontal patterns of the 850-hPa wind (vector, unit: m s^{-1}) and temperature (shaded, unit: K) fields regressed onto the standardized time series of the leading EOF mode of the 850-hPa synoptic-scale meridional wind in the 30°-60° latitudinal band.

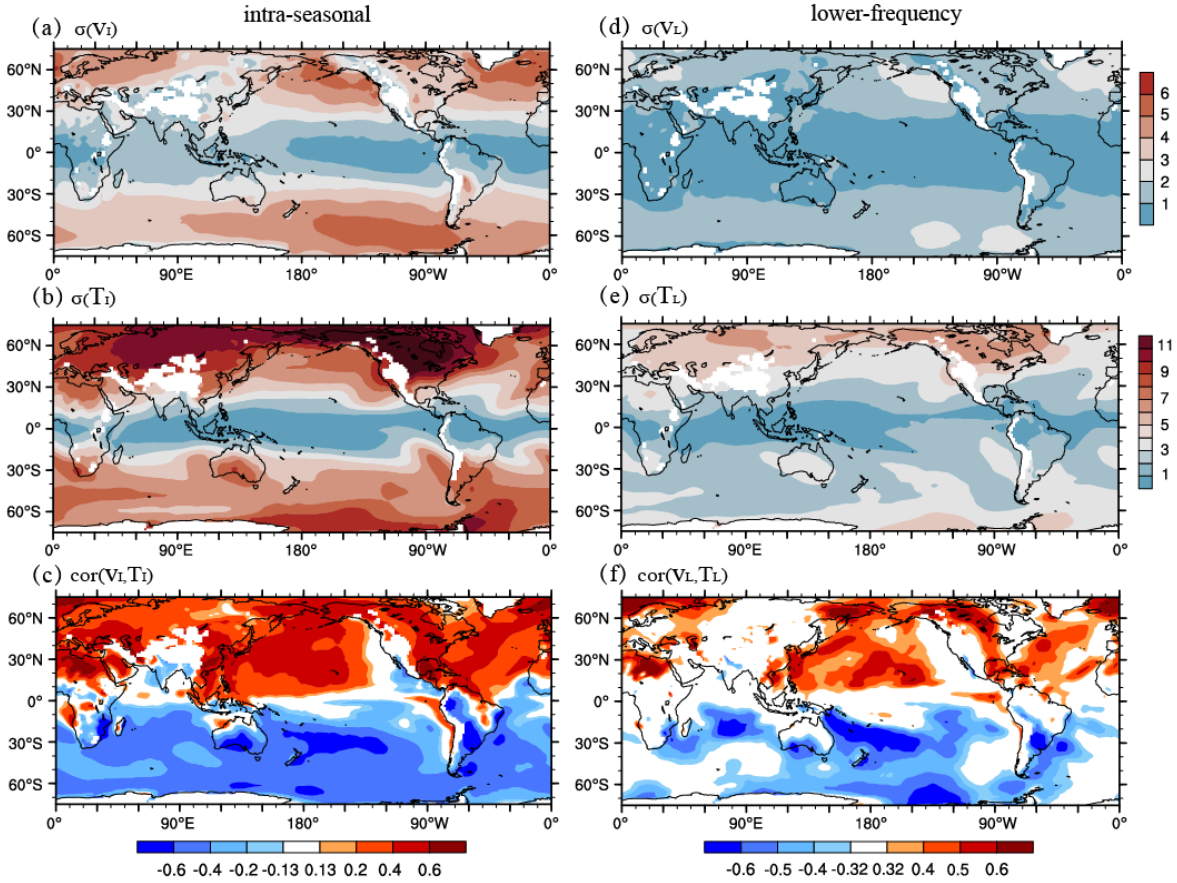

FIGURE 6 As in Figure 4 (a)-(c) except for (left) the intra-seasonal and (right) lower-frequency modes.

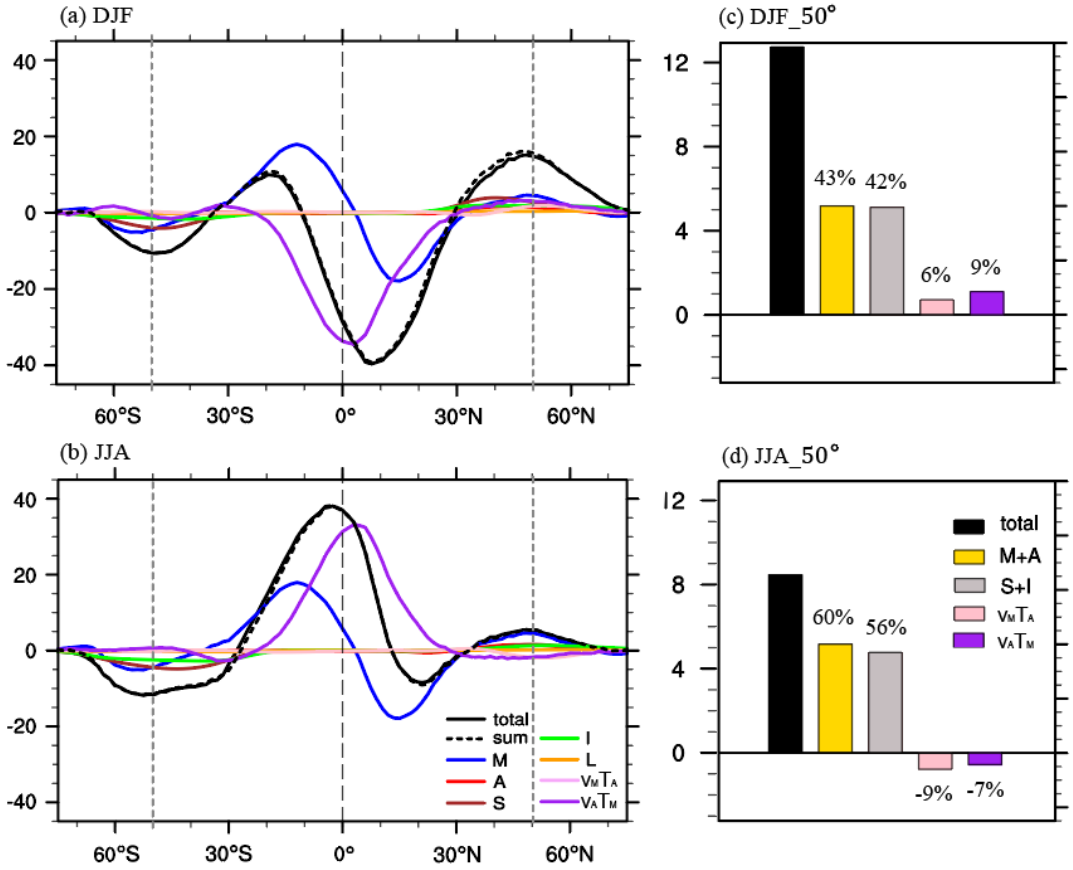

FIGURE 7 As in Figure 1 except for the vertically integrated seasonal mean meridional heat flux in (a, c) DJF and (b, d) JJA. The purple curve and bar denote the heat flux associated with the interaction between the seasonal anomalous meridional wind and the climatological annual mean temperature ($v_A T_M$), the pink curve and bar denote the heat flux associated with the interaction between the climatological annual mean meridional wind and the seasonal anomalous temperature ($v_M T_A$), and the black dashed curve represents the sum of the seven components (M, A, S, I, L, $v_A T_M$, and $v_M T_A$).

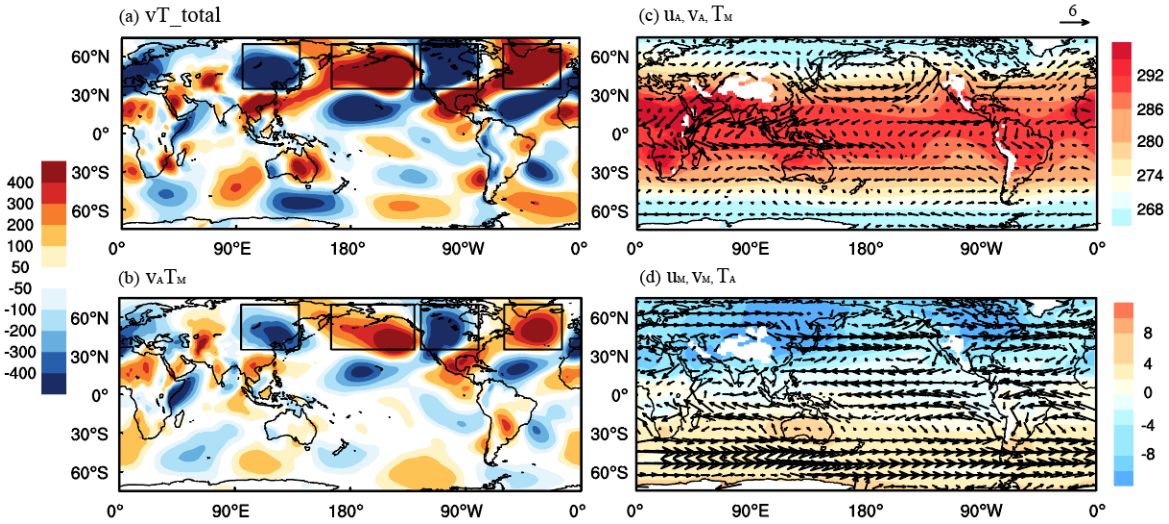

FIGURE 8 (a) Vertically integrated seasonal mean meridional heat flux (unit: 10^4 K kg m^{-1} s^{-1}) in DJF during 1981-2015. (b) As in (a) except for the heat flux due to the interaction between the seasonal anomalous meridional wind and the climatological annual mean temperature. Horizontal patterns of the 850-hPa (c) seasonal anomalous wind (vector, unit: m s^{-1}) in DJF and the climatological annual mean temperature (shaded, unit: K) and (d) climatological annual mean wind (vector, unit: m s^{-1}) and the seasonal anomalous temperature (shaded, unit: K) in DJF. The black boxes in (a, b) represent the key regions for the wave train pattern of the meridional heat transport in the mid-latitude NH.

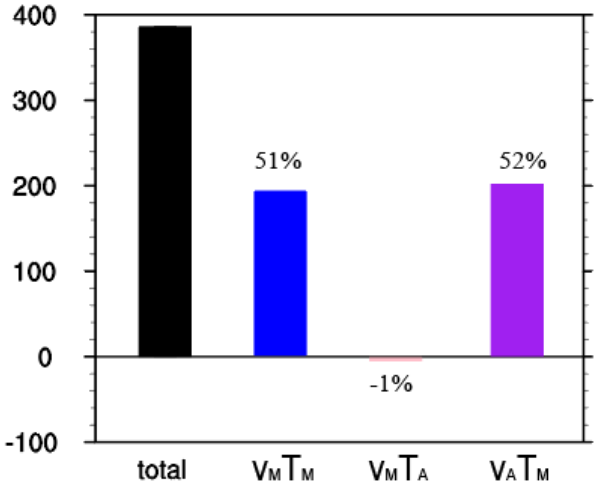

FIGURE 9 Averaged meridional heat flux (unit: 10^4 K kg m^{-1} s^{-1}) and relative percentage contributions by the climatological annual mean circulations (blue), the interaction between the climatological annual mean meridional wind and the seasonal anomalous temperature (pink), and the interaction between the climatological annual mean temperature and the seasonal anomalous meridional wind (purple) in the four key regions (black boxes in Figure 8) for the wave train pattern of the meridional heat transport in the NH in DJF. The black bar denotes the averaged total heat flux.

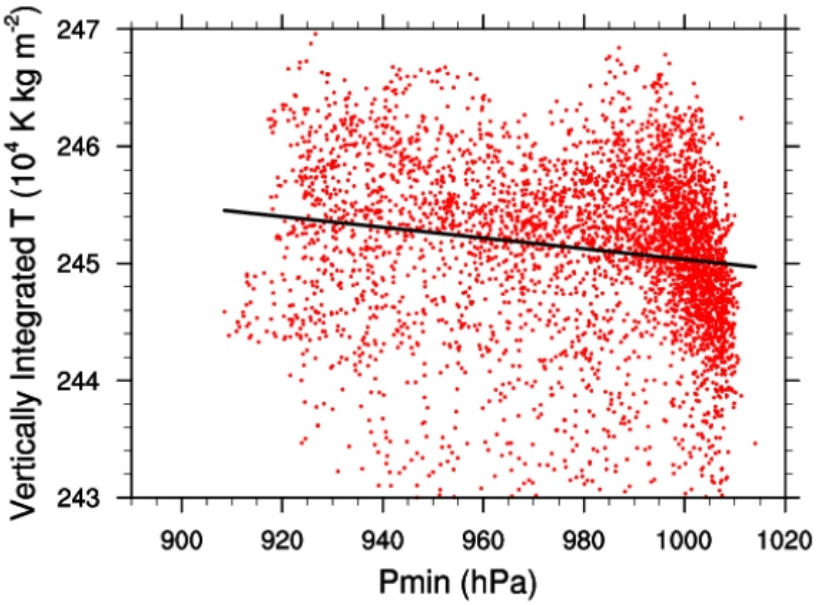

FIGURE 10 Scatter diagrams between the vertically integrated temperature (unit: 10^4 K kg m^{-2}; red dots) averaged within a 500-km radius from the TC center and the TC minimum sea level pressure (unit: hPa). The slope of the linear regression line (black line) exceeds a 99% confidence level based on Student's t-test.

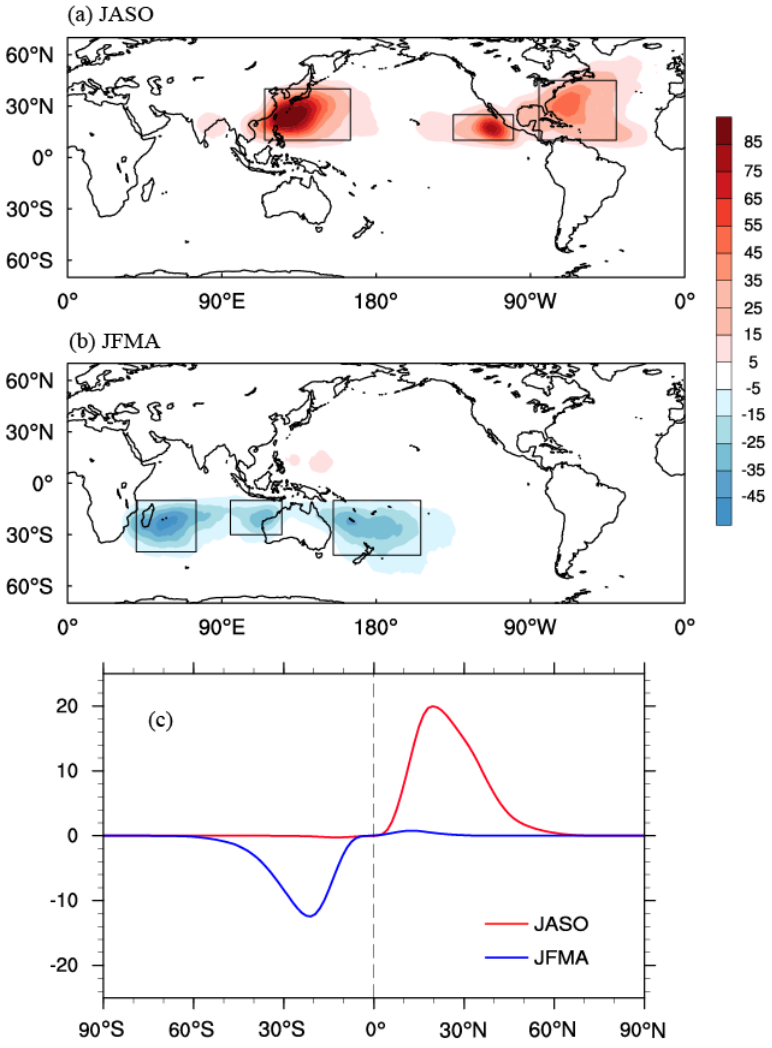

FIGURE 11 Horizontal patterns of the vertically integrated TC-induced heat flux (unit: 10^4 K kg m^{-1} s^{-1}) in (a) JASO and (b) JFMA 1981-2015. (c) Zonal mean meridional heat flux by TCs in JASO (red) and JFMA (blue). The black boxes in (a, b) represent the major regions for TC heat transport in the WNP (10ºN-40ºN, 115ºE-165ºE), ENP (10ºN-25ºN, 135ºW-100ºW), NA (10ºN-45ºN, 85ºW-40ºW), SIO (10ºS-40ºS, 40ºE-75ºE), Australia (10ºS-30ºS, 95ºE-125ºE), and SP (10ºS-40ºS, 155ºE-155ºW).

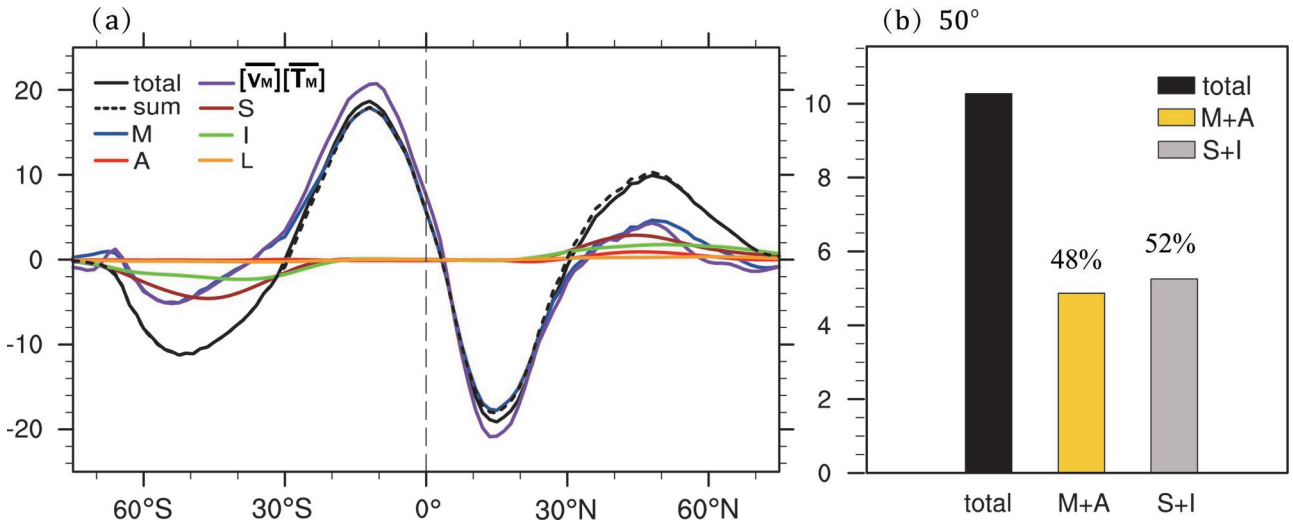

joc_7357_fig. 1.eps

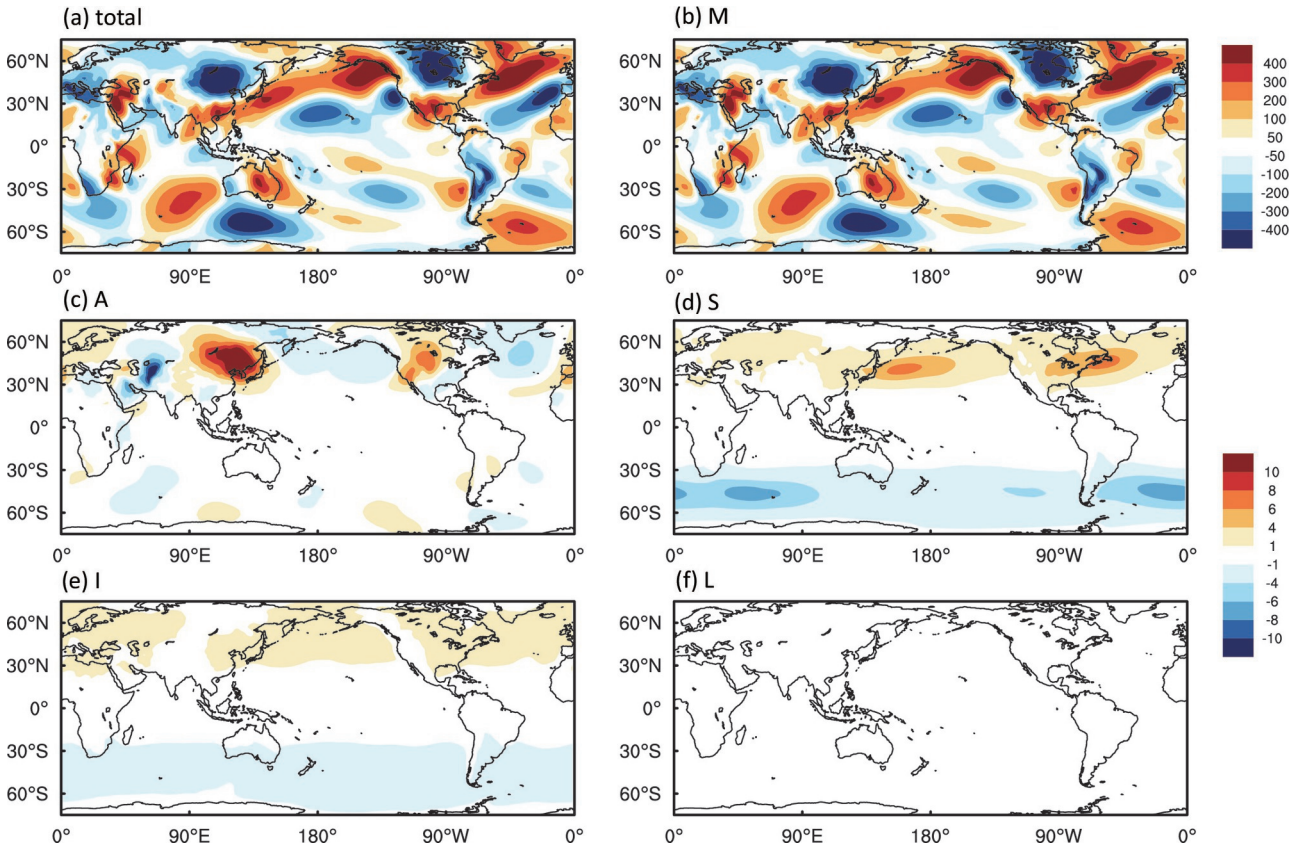

joc_7357_fig. 2.eps

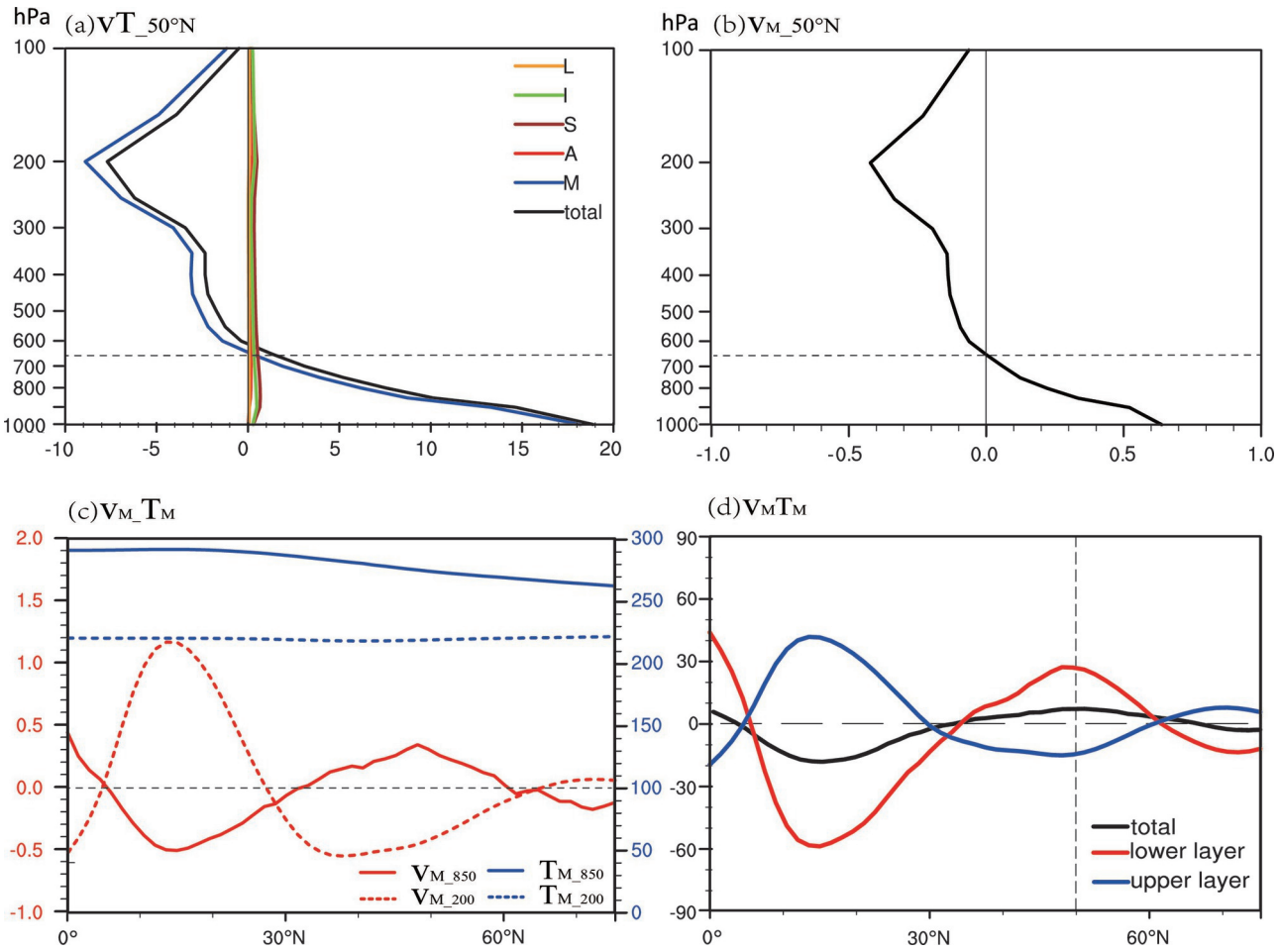

joc_7357_fig. 3.eps

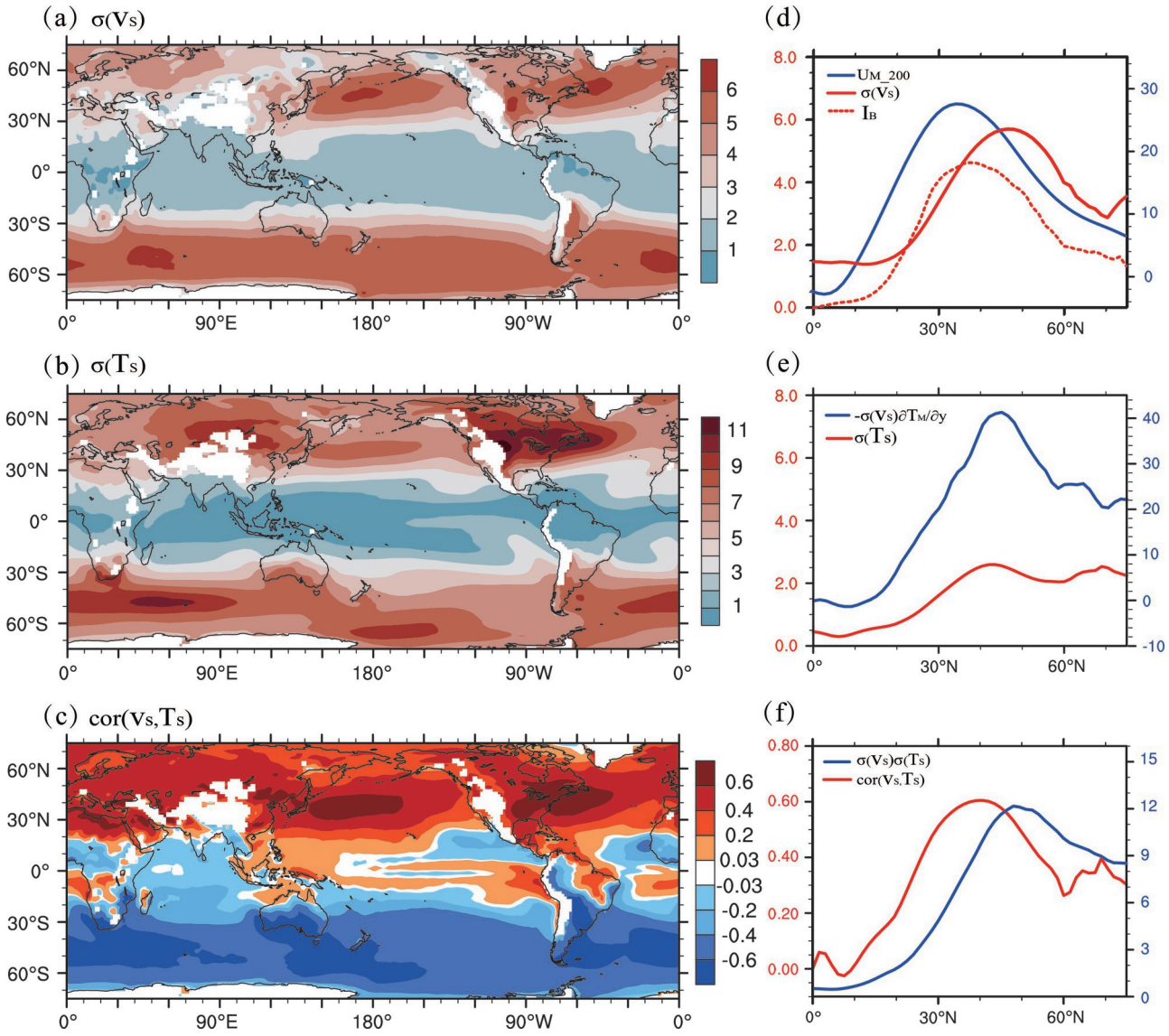

joc_7357_fig. 4.eps

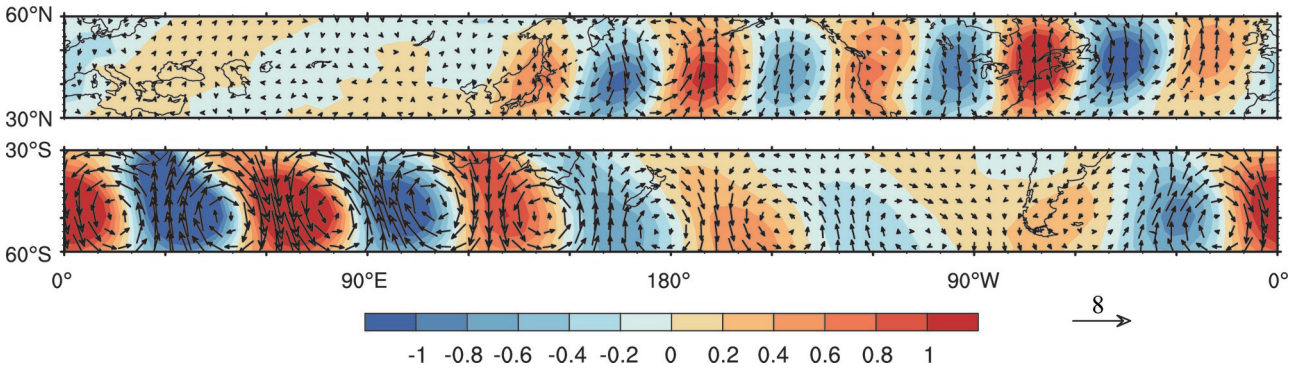

joc_7357_fig. 5.eps

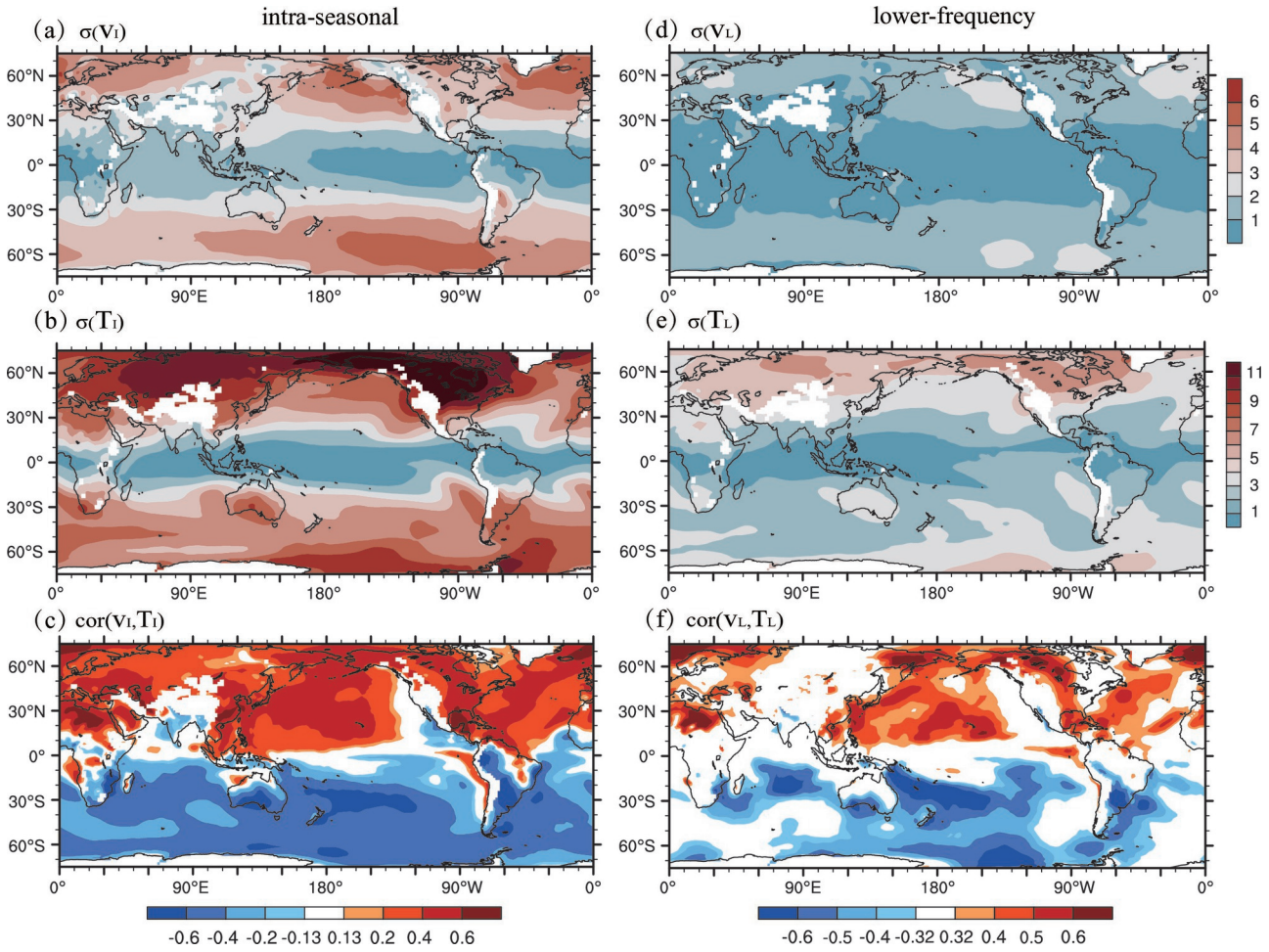

joc_7357_fig. 6.eps

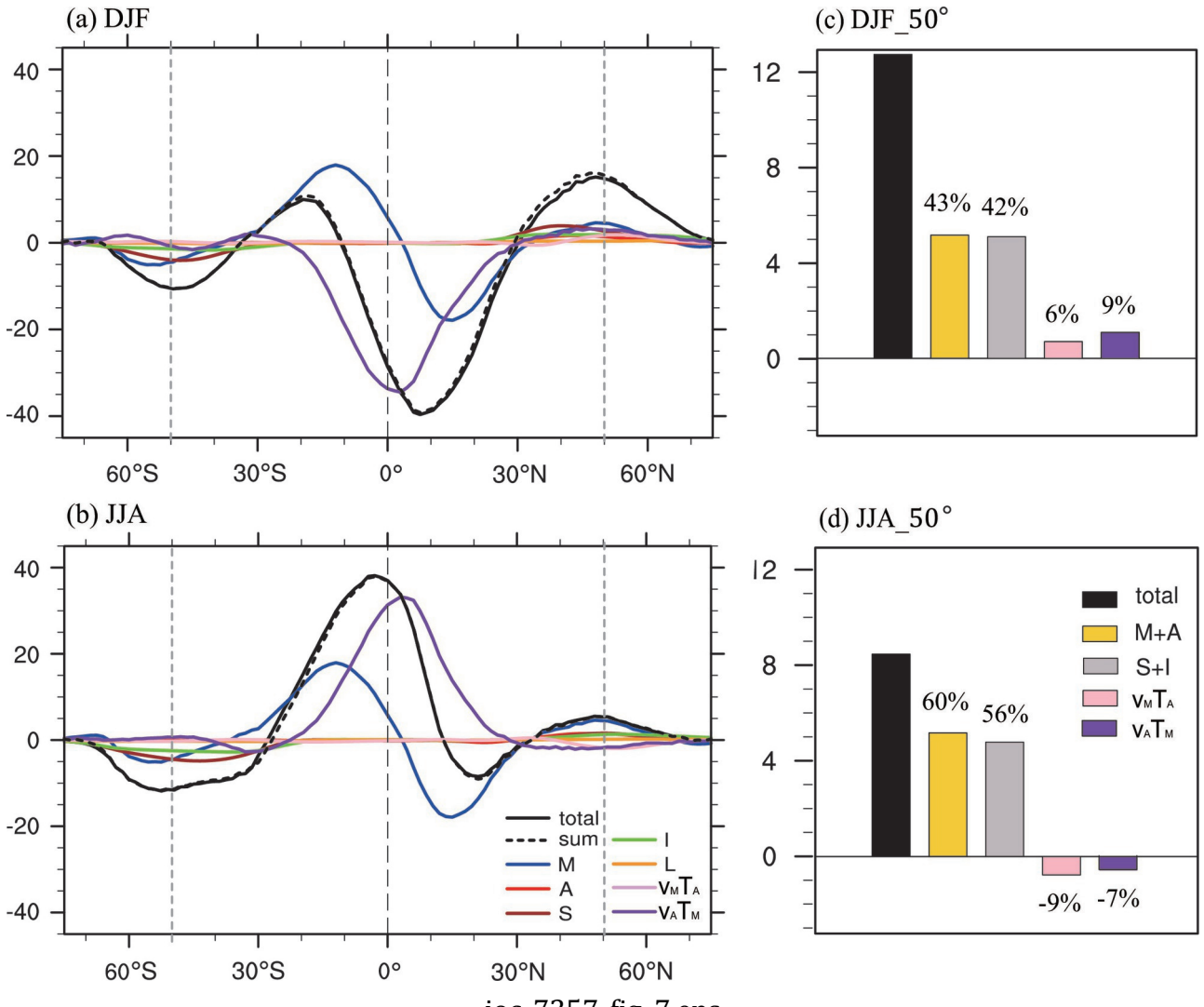

joc_7357_fig. 7.eps

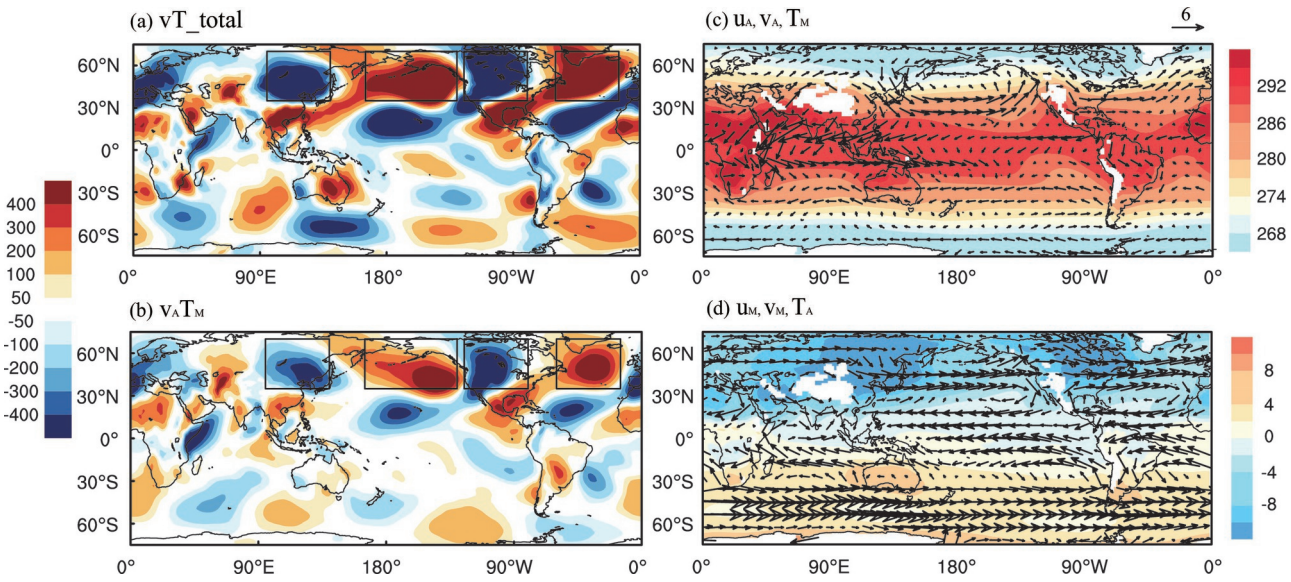

joc_7357_fig. 8.eps

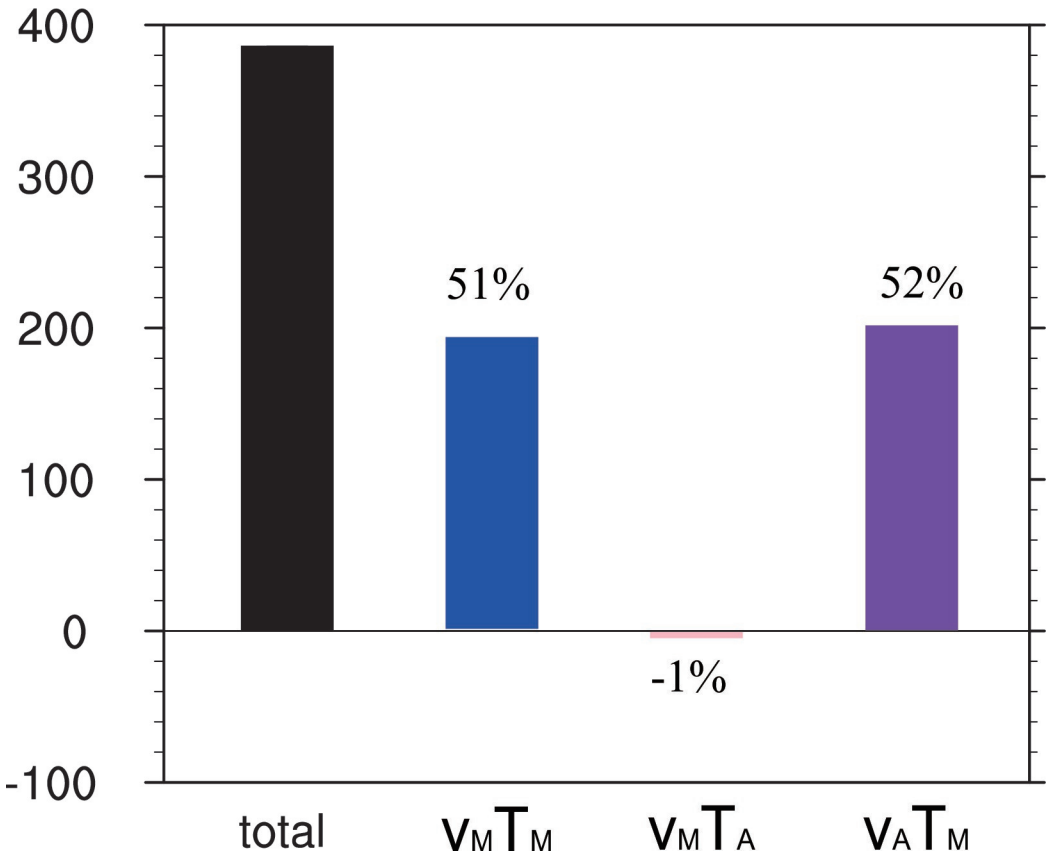

joc_7357_fig. 9.eps

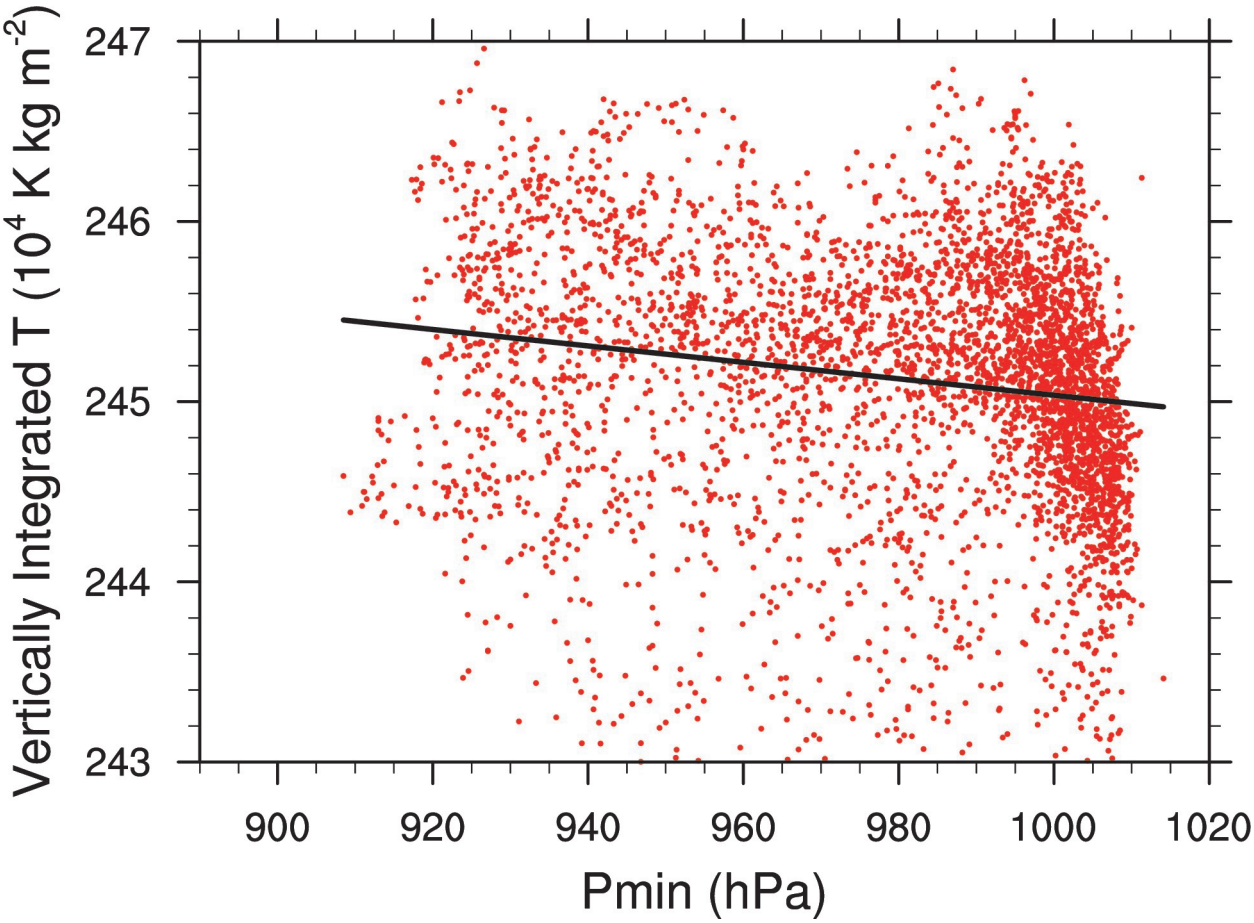

joc_7357_fig. 10.eps

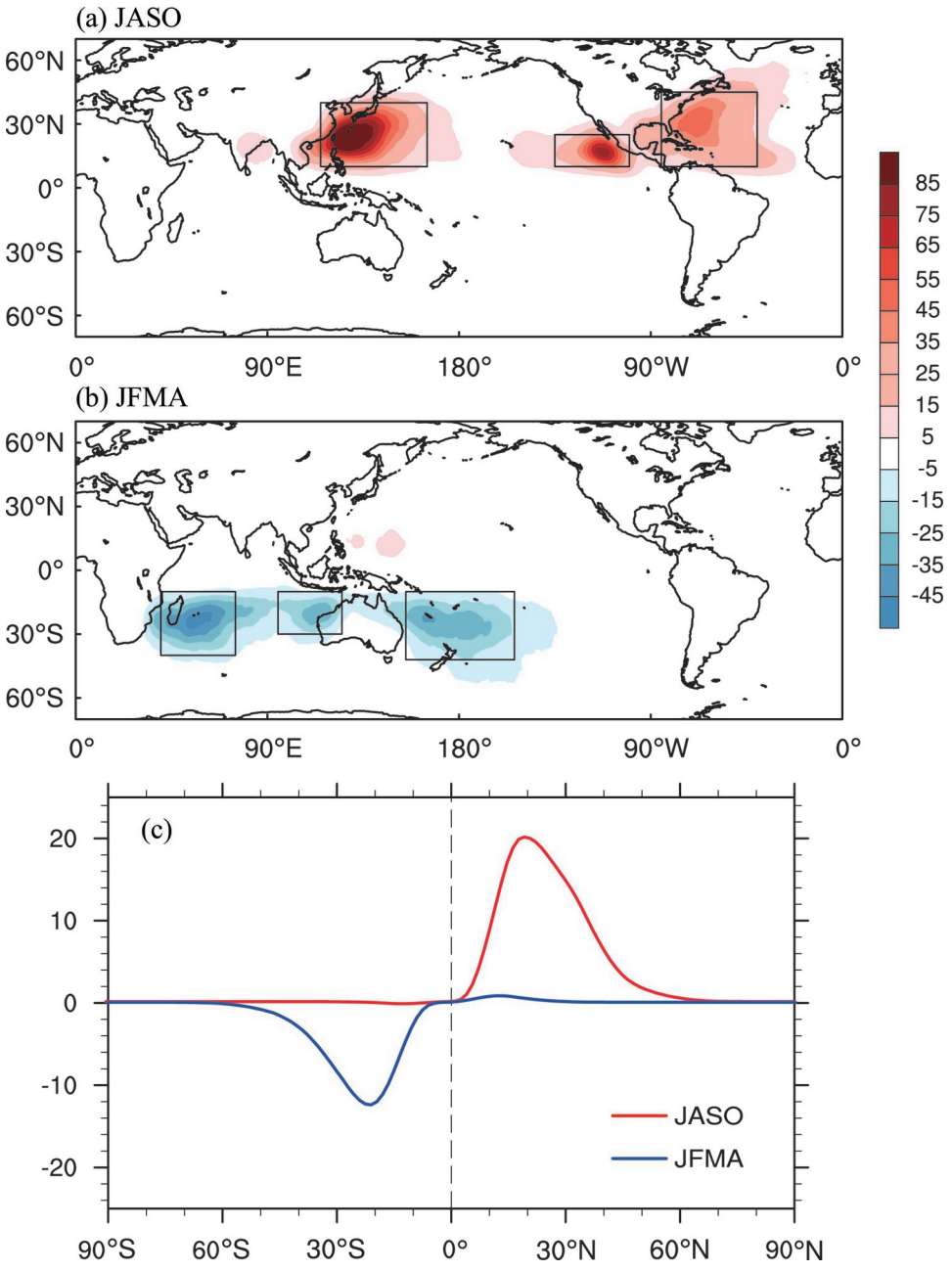

joc_7357_fig. 11.eps

Impacts of Multi-timescale Circulations on Meridional Heat Transport

Qiao LIU, Tim LI*, and Weican ZHOU

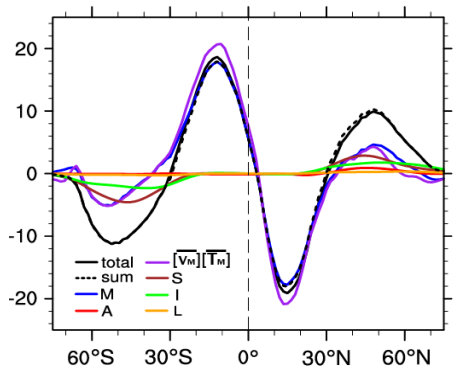

In the tropics, the climatological annual mean circulations dominate the long-term mean meridional heat transport, while the interaction between the climatological annual mean temperature and the seasonal anomalous flow largely contributes to the seasonal variation of the meridional heat transport. In the middle latitudes, the climatological annual mean circulations and transient eddies (mostly synoptic and intra-seasonal eddies) are of roughly equal importance in the poleward heat transport, leading to the maximum poleward heat transport around 50°N/S.